Multi-component vapor-liquid equilibrium model for LES of high-pressure fuel injection and application to ECN Spray A

Matheis, Jan; Hickel, Stefan

DOI
10.1016/j.ijmultiphaseflow.2017.11.001

Publication date
2018

Document Version
Final published version

Published in
International Journal of Multiphase Flow

Citation (APA)
Matheis, J., & Hickel, S. (2018). Multi-component vapor-liquid equilibrium model for LES of high-pressure fuel injection and application to ECN Spray A. *International Journal of Multiphase Flow*, *99*, 294-311. https://doi.org/10.1016/j.ijmultiphaseflow.2017.11.001

International Journal of Multiphase Flow 99 (2018) 294–311

Contents lists available at ScienceDirect

International Journal of Multiphase Flow

journal homepage: www.elsevier.com/locate/ijmulflow

Multi-component vapor-liquid equilibrium model for LES of high-pressure fuel injection and application to ECN Spray A

Jan Matheis[a,*], Stefan Hickel[b]

[a] Chair of Aerodynamics and Fluid Mechanics, Department of Mechanical Engineering, Technical University of Munich, Boltzmannstr. 15, Garching 85747, Germany

[b] Chair of Aerodynamics, Faculty of Aerospace Engineering, Technische Universiteit Delft, P.O. Box 5058, 2600 GB Delft, The Netherlands

ARTICLE INFO

Article history:
Received 15 February 2017
Revised 19 August 2017
Accepted 1 November 2017
Available online 8 November 2017

Keywords:
Diesel fuel injection
Engine Combustion Network (ECN) Spray A
Large Eddy Simulation (LES)
Vapor-liquid equilibrium (VLE)
Supercritical
Transcritical

ABSTRACT

We present and evaluate a two-phase model for Eulerian large-eddy simulations (LES) of liquid-fuel injection and mixing at high pressure. The model is based on cubic equations of state and vapor-liquid equilibrium calculations and can represent the coexistence of supercritical states and multi-component subcritical two-phase states via a homogeneous mixture approach. Well-resolved LES results for the Spray A benchmark case of the Engine Combustion Network (ECN) and three additional operating conditions are found to agree very well with available experimental data. We also address well-known numerical challenges of trans- and supercritical fluid mixing and compare a fully conservative formulation to a quasi-conservative formulation of the governing equations. Our results prove physical and numerical consistency of both methods on fine grids and demonstrate the effects of energy conservation errors associated with the quasi-conservative formulation on typical LES grids.

1. Introduction

We present and analyze novel physical and numerical models for the large-eddy simulation (LES) of high-pressure liquid-fuel injection and the turbulent mixing of subcritical and supercritical fluids at conditions typical for liquid rocket engines, modern diesel engines and gas turbines. A representative application example is the Spray A benchmark case of the Engine Combustion Network (ECN). The baseline setup consists of a cold n-dodecane jet ($C_{12}H_{26}$ at 363 K) that is injected with about 600 m/s into a warm nitrogen (N_2) atmosphere at $T = 900$ K and a pressure of $p = 6$ MPa. This high pressure exceeds the critical pressure p_c of both components and results in a compressed liquid ($p > p_c,\ T < T_c$) and a gas-like ($T > T_c,\ p > p_c$) state of the two pure species. However, the critical pressure of certain mixtures of the two species is much higher than the critical pressure of the pure species and also higher than the Spray A operating pressure, such that the mixture locally enters a two-phase region and interfaces between liquid and gas phases may appear during the mixing process.

The ECN Spray A have received considerable attention in the community since experimental and theoretical findings, see, e.g., Dahms et al. (2013) and Dahms and Oefelein (2013), questioned the established paradigm of classic spray atomization (primary and secondary breakup, evaporation of droplets) for high-pressure and high-temperature fuel injection: above certain pressures and temperatures a *dense fluid mixing* with diminishing surface tension was observed in the near-field of n-dodecane sprays after the end of injection (EOI), see, e.g., Manin et al. (2014). With improved optical diagnostics, Crua et al. (2015, 2017) pushed recently the boundaries above which this transition takes place towards higher pressures and temperatures. Hence, the nominal operating conditions of Spray A now seem to be more within the subcritical regime. Moreover, their measurements showed that the fluid does not reach the *dense-fluid mixing* state instantaneously and classical evaporation does occur for some time. Therefore, classical two-phase phenomena appear to be relevant for high-pressure and high-temperature fuel injection and must be taken into account by the physical models employed for Spray A simulations.

Previous numerical simulations of Spray A have modeled the spray with Lagrangian particle tracking (LPT) methods, i.e., as a classical two-phase spray with sharp gas-liquid interfaces evolving according to models for first- and secondary breakup and evaporation, using either Reynolds-Average Navier-Stokes (RANS) (Pei et al. (2015a)) or LES formulations (Jangi et al. (2015); Pei et al. (2015b); Senecal and Pomraning (2014); Wehrfritz et al. (2013); Xue et al. (2013)). While LPT methods yield impressive results for dilute

* Corresponding author.
E-mail addresses: jan.matheis@tum.de (J. Matheis), S.Hickel@tudelft.nl (S. Hickel).

https://doi.org/10.1016/j.ijmultiphaseflow.2017.11.001

two-phase flows, i.e., for flows where droplet interactions are rare and the droplet volume fraction is very small, they have shortcomings when applied to very dense flow regimes near the nozzle, where the liquid fuel disintegrates into ligaments and further into droplets. Here, semi-empirical Lagrangian primary-breakup models or assumptions on initial droplet size distributions are used, which then render LPT methods sensitive to calibration parameters. Note that quantitative experimental droplet size measurements are usually not available for high-pressure high-temperature sprays.

Intuitively, it appears to be easier to represent primary atomization in an Eulerian framework. Very high injection pressures and injection velocities also suggest that compressibility effects should be taken into account. Numerical simulations of Spray A that take advantage of such a fully compressible Eulerian framework for primary atomization have recently been presented by Lacaze et al. (2015) and Hakim et al. (2016), using the Peng–Robinson (PR) equation of state (EOS) in an assumed single-phase dense-gas approach (supported by experimental findings at that time). Their results underline the importance of real-gas effects, e.g., speed of sound or specific heat peculiarities, in high-pressure fuel injection systems. The single-phase dense-gas approach, however, does not include the effect of phase separation. This may lead to unphysical or ill-defined states, caused by the cubic EOS and mixing rule framework, if part of the flow is governed by classical two-phase theory. More recently, Knudsen et al. (2016) reproduced impressively nozzle mass and momentum fluxes for Spray A by using also a fully compressible Eulerian PR EOS based approach for the LES of internal nozzle flow and downstream reservoir in a single domain. To keep computational costs tractable they rely on the dense-fluid mixing concept but apply a novel and simplified approach for describing the saturation line in a pressure-volume diagram. As noted by Knudsen et al. (2016), a thermodynamically consistent description of mixture thermodynamics adds significant cost to the overall solver. In the light of increasing computational power and driven by the idea to increase the level of thermodynamic consistency for LES of high-pressure fuel-injection applications, we have developed a thermodynamically consistent detailed multi-species two-phase model for the Eulerian LES of turbulent mixing under high pressures (Matheis and Hickel, 2016). The thermodynamics model is based on cubic EOS and vapor-liquid equilibrium (VLE) calculations. For a homogenous mixture it can represent multi-component supercritical states as well as coexisting multi-component subcritical two-phase states in a computational cell without empirical tuning parameters. We want to emphasize that this model is inspired by the work of Qiu and Reitz (2014, 2015), who apply a similar approach in the context of RANS simulations.

LES of high-pressure fuel injection is also very challenging with respect to numerical stability. The reasons are manifold: we see density ratios larger than 30 across the mixing layer, hydrodynamic pressure fluctuations in the order of magnitude of 10 bar, and locally even supersonic flow (as also reported by Lacaze et al. (2015)). Moreover, it is known that a fully conservative (FC) formulation of the governing equations together with a nonlinear real-gas EOS may lead to spurious pressure oscillations in the flow field, which can deteriorate computational stability, see, e.g., Refs. Terashima and Koshi (2012), Terashima and Koshi (2015) and Ma et al. (2014, 2016). Abgrall and Karni (2001) describe a similar problem well-known in compressible ideal gas multi-component flows. Recently, Terashima and Koshi (2012, 2015) presented a numerical approach, specifically designed for LES of mixing under such harsh conditions, for which the total energy conservation equation is replaced by a pressure-evolution equation. This leads to a quasi-conservative (QC) formulation, where energy is not exactly conserved. We present a comparison of QC and FC LES results for Spray A which allows us to distinguish between physical and numerical pressure fluctuations and to draw a conclusion on the effects of energy conservation errors associated with a QC formulation on typical LES grids.

The remainder of the paper proceeds as follows: In Section 2 we introduce the physical and numerical models, i.e., the governing equations in FC and QC formulation, the multi-component two-phase thermodynamic model, the employed turbulence model and discretization method. A validation of the PR EOS in comparison to experimental VLE data together with an analytical evaluation of the thermodynamic models is presented in Section 3. Consistency and convergence of the FC and QC discretization of the governing equations is proved in Section 4 for a 1-D test case at thermodynamic conditions similar to Spray A. Results for LES of Spray A are discussed in Section 5. In Section 6, we present the first LES results for three additional operating points. The paper will end in Section 7 with a discussion and outlook.

2. Physical and numerical models

2.1. Governing equations

We solve the three-dimensional compressible multi-component Navier-Stokes equations either in a fully conservative (FC) formulation,

$$\partial_t \rho + \nabla \cdot (\rho \mathbf{u}) = 0 \tag{1}$$

$$\partial_t \rho Y_i + \nabla \cdot (\rho Y_i \mathbf{u}) = \nabla \cdot \mathbf{J}_i \tag{2}$$

$$\partial_t \rho \mathbf{u} + \nabla \cdot (\rho \mathbf{u}\mathbf{u} + \mathbf{I}p) = \nabla \cdot \boldsymbol{\tau} \tag{3}$$

$$\partial_t E + \nabla \cdot [(E + p)\mathbf{u}] = \nabla \cdot (\mathbf{u} \cdot \boldsymbol{\tau} - \mathbf{q}), \tag{4}$$

or in a quasi-conservative (QC) formulation for which the total energy conservation, Eq. (4), is replaced by the pressure-evolution equation

$$\begin{aligned} \partial_t p + \nabla \cdot (p\mathbf{u}) = {} & (p - \rho c^2)\nabla \cdot \mathbf{u} \ldots \\ & + \frac{\alpha_p}{c_v \beta_T \rho}[\nabla \cdot (\boldsymbol{\tau} \cdot \mathbf{u} - \mathbf{q}) - \mathbf{u} \cdot (\nabla \cdot \boldsymbol{\tau})] \ldots \\ & + \sum_{i=1}^{N_c} \frac{1}{\rho} \frac{\partial p}{\partial Y_i}\bigg|_{\rho, e, Y_{j \neq i}} \nabla \cdot \mathbf{J}_i. \end{aligned} \tag{5}$$

The state vector consists of mass density ρ, partial densities ρY_i of species $i = \{1 \ldots N_c\}$, linear momentum $\rho\mathbf{u}$, and total energy density $E = \rho e + \frac{1}{2}\rho \mathbf{u} \cdot \mathbf{u}$ (FC) or pressure p (QC). $\mathbf{u} = [u_1, u_2, u_3]^T$ is the velocity vector in a Cartesian frame of reference, c denotes the speed of sound, c_v is the heat capacity at constant volume, and α_p and β_T are the thermal expansion and isothermal compressibility coefficient. To allow for a meaningful comparison between FC and QC simulations, we also included the effect of the diffusion induced pressure variation, the last term on the right-hand side of Eq. (5), which was neglected in Ref. Terashima and Koshi (2012). The non-trivial thermodynamic derivative is calculated as

$$\frac{\partial p}{\partial Y_i}\bigg|_{e, \rho, Y_{j \neq i}} = -\frac{\partial p}{\partial e}\bigg|_{Y_j, \rho} \cdot \frac{\partial e}{\partial Y_i}\bigg|_{p, \rho, Y_{j \neq i}} \tag{6}$$

with

$$\frac{\partial e}{\partial Y_i}\bigg|_{p, \rho, Y_{j \neq i}} = h_i - \frac{c_p}{v\,\alpha_p} v_i, \tag{7}$$

cf., Okong'o and Bellan (2002). The two terms on the right-hand side of Eq. (7), h_i and v_i, are known as partial enthalpy and partial volume (on a mass basis) of species i. Helpful details on the calculation of partial properties can be found in Elliott and Lira (2012) and Masquelet (2013). For a more detailed discussion on Eq.

(5) it is referred to the original work of Terashima and Koshi (2012, 2015).

According to Stokes' hypothesis for a Newtonian fluid, the viscous stress tensor is

$$\boldsymbol{\tau} = \mu\left(\boldsymbol{\nabla}\mathbf{u} + (\boldsymbol{\nabla}\mathbf{u})^T - 2/3\,\mathbf{I}\,\boldsymbol{\nabla}\cdot\mathbf{u}\right), \tag{8}$$

with μ being the dynamic viscosity and $\mathbf{I}$ the unit tensor. We note that there are strong reasons to believe that Stokes' hypothesis is not valid close to the critical point. Effects of bulk viscosity are, nevertheless, neglected in this paper because sufficiently general and accurate models are, to our knowledge, not available. The diffusional fluxes are calculated via Fick's law

$$\mathbf{J}_i = \rho D_i \boldsymbol{\nabla} Y_i - Y_i \sum_{j=1}^{N_c} \rho D_j \boldsymbol{\nabla} Y_j \ , \tag{9}$$

where

$$D_i = \frac{(1 - z_i)}{\sum_{j\neq i}^{N_c} \frac{z_j}{D_{ij}}} \tag{10}$$

is an effective binary diffusion coefficient for the diffusion of species i into the rest of the mixture, and z_i denotes the overall mole fraction of species i. The physical binary mass diffusion coefficients D_{ij} are modeled according to Chapman and Enskog theory, see, e.g., Chapter 11-3 in Poling et al. (2000). The vector

$$\mathbf{q} = -\kappa \boldsymbol{\nabla} T \ - \sum_{i=1}^{N_c} h_i \mathbf{J}_i \tag{11}$$

consists of heat conduction and the enthalpy flux by species diffusion, where κ is the thermal conductivity, T is the temperature, and h_i is the partial enthalpy of species i. Viscosity and thermal conductivity are modeled with correlations given by Chung et al. (1988).

Eqs. (1)–(4) describe the general conservation laws for mass, momentum and energy. We solve these equations with a finite-volume (FV) method that uses a single-fluid approach to describe single-phase liquids and gases as well as two-phase mixtures, see Section 2.4. With a single-fluid FV method, all quantities represent local volume averages and individual interfaces are not resolved. The phase composition of the fluid enters these equations through the thermodynamic model that relates internal energy and partial densities to pressure, temperature and transport properties. Our model for multi-component subcritical and supercritical states is based on the following underlying assumptions:

- The fluid within a computational cell is in local thermodynamic equilibrium.
- Phase interfaces are in mechanical equilibrium and surface tension effects can be neglected.
- There is a single-valued subgrid-scale velocity for both phases (no-slip).

The first assumption implies that the time required to reach local thermodynamic equilibrium (in terms of pressure, temperature and phase composition) in response to transport processes has to be much smaller than the numerically resolved hydrodynamic time scales and preferably smaller than the computational time step. The second assumptions limits the model to high Weber number flows, which is typically the case in high-pressure injection. The third assumption implies that the inertia time scale of unresolved droplets and bubbles is smaller than the numerically resolved hydrodynamic time scales, that is, the Stokes number of droplets that are smaller than the mesh size must be low. With sufficient mesh resolution, however, the model can be also used to perform well resolved simulations of droplets with arbitrary inertia time scales. The vaporization time scale is then obviously also limited by the transport of heat, but not by surface tension unless an explicit model is added. The present approach yields a unified and parameter-free framework valid for both multi-component subcritical two-phase states and also multi-component supercritical states. A comparison with experimental results in Sections 5 and 6 will provide a justification for applying the homogeneous mixture methodology for LES of high-pressure and high-temperature sprays.

Table 1
Critical properties and acentric factor of nitrogen and n-dodecane.

Species	T_c [K]	p_c [Pa]	ω [-]
N_2	126.192	3.3958×10^6	0.0372
$C_{12}H_{26}$	658.0	1.8200×10^6	0.5764

2.2. Multi-component single-phase equation of state

The equations presented in this subsection are valid for a homogeneous fluid phase composed of an arbitrary number of components $N_c \geq 1$. The single- and two-phase models are based on cubic EOS

$$p(\underline{v}, T, \mathbf{z}) = \frac{\mathcal{R}T}{\underline{v} - b} - \frac{a\alpha}{\underline{v}^2 + u\,b\,\underline{v} + wb^2}, \tag{12}$$

where the pressure p is a function of the molar volume $\underline{v}$, temperature T and the molar composition $\mathbf{z} = \{z_1, \cdots, z_{N_c}\}$. Here and in the following, all intensive thermodynamic properties are expressed as molar quantities, denoted by $\underline{\star}$. $\mathcal{R}$ is the universal gas constant. In all subsequent simulations we use the Peng–Robinson (PR) EOS (Peng and Robinson, 1976) for which $u = 2$ and $w = -1$. The function

$$\alpha = [1 + c_0(1 - \sqrt{T_r})]^2 \quad \text{with} \quad T_r = T/T_c \tag{13}$$

accounts for the polarity of a fluid and is a correlation of temperature T, critical temperature T_c and acentric factor ω via

$$c_0 = 0.37464 + 1.54226\omega - 0.2699\omega^2. \tag{14}$$

$T_r = T/T_c$ is known as the reduced temperature. The parameter $a = 0.45724\left(\mathcal{R}^2 T_c^2 / p_c\right)$ represents attractive forces between molecules and the effective molecular volume is represented by $b = 0.0778(\mathcal{R}T_c/p_c)$. The critical properties and the acentric factor of nitrogen and n-dodecane are given in Table 1.

We use conventional mixing rules to extend the PR EOS to a mixture composed of N_c components. The parameters required in the EOS are calculated from

$$a\alpha = \sum_i^{N_c} \sum_j^{N_c} z_i z_j a_{ij} \alpha_{ij} \quad \text{and} \quad b = \sum_i^{N_c} z_i b_i, \tag{15}$$

with z_i being the mole fraction of component i (overall or in the liquid/vapor phase). The coefficients a_{ij} and α_{ij} are calculated with pseudo-critical combination rules, see, .e.g., Reid et al. (1987) in Chapter 4: off-diagonal elements are calculated using the same expression as for the diagonals together with pseudo-critical parameters

$$\begin{aligned} T_{c,ij} &= \sqrt{T_{c,i} T_{c,j}}(1 - k'_{ij}), \quad p_{c,ij} = Z_{c,ij}(\mathcal{R}T_{c,ij}/v_{c,ij}), \\ v_{c,ij} &= \frac{1}{8}\left[v_{c,i}^{1/3} + v_{c,j}^{1/3}\right]^3, \\ \omega_{ij} &= 0.5\left(\omega_i + \omega_j\right) \quad \text{and} \quad Z_{c,ij} = 0.5\left(Z_i + Z_j\right). \end{aligned} \tag{16}$$

As pointed out by Reid et al. (1987), it is important to realize that mixing- and combining rules are essentially empirical. Only a comparison against experimental VLE or pressure-volume-temperature (PVT) data can give confidence that the employed mixture model is appropriate for the calculation of volumetric mixture properties.

In this work, the binary interaction parameter k'_{ij} is set to zero. The accuracy of this approach will be addressed in Section 3.

In addition to the thermal EOS, expressions for caloric properties (e.g., internal energy $\underline{e}$, specific heats $\underline{c}_p$ and $\underline{c}_v$, etc.) that account for their pressure dependance are needed. The departure function formalism provides such expressions and only requires relationships provided by the EOS. The departure function, e.g., for the internal energy, can be written as

$$\underline{e}(T,\underline{v},\mathbf{z}) = \underline{e}^{ig}(T,\mathbf{z}) + \int_{\infty}^{\underline{v}} \left[T \left.\frac{\partial p}{\partial T}\right|_{\underline{v}} - p \right] d\underline{v}. \tag{17}$$

Using the generalized cubic EOS (Eq. 12), the solution of the integral reads

$$\left(\underline{e} - \underline{e}^{ig}\right) = \frac{1}{b\sqrt{u^2-4w}} \left[a\alpha - T\frac{\partial a\alpha}{\partial T} \right] \ln\left[\frac{2\underline{v} + ub - b\sqrt{u^2-4w}}{2\underline{v} + ub + b\sqrt{u^2-4w}} \right]. \tag{18}$$

The ideal reference state denoted by the superscript ^{ig} is evaluated using the 9-coefficient NASA polynomials (Goos et al., 2009). Analytical solutions to other caloric properties are available in literature, see, e.g., Poling et al. (2000).

The single-phase frozen temperature T_F (following the notation of Qiu and Reitz (2015)) is computed iteratively by minimizing the objective function

$$F^{FC} = \frac{\underline{e}^\star - \underline{e}_F(T_F,\underline{\rho}^\star,\mathbf{z}^\star)}{\underline{e}_{norm}} \text{ or } F^{QC} = \frac{p^\star - p(T_F,\underline{\rho}^\star,\mathbf{z}^\star)}{p^\star}, \tag{19}$$

with $\underline{e}^\star = \underline{e}_{LES}$ (FC), $p^\star = p_{LES}$ (QC), $\underline{\rho}^\star = \underline{\rho}_{LES}$ and $\mathbf{z}^\star = \mathbf{z}_{LES}$ being the molar internal energy, pressure, molar density and overall molar composition that come from the flow solver (after conversion to molar quantities). To avoid division by zero the normalization reads $\underline{e}_{norm} = \underline{e}^\star$ if $|\underline{e}^\star| > 1$, else $\underline{e}_{norm} = 1$. Once the temperature is available, all other thermodynamic properties (e.g., pressure for FC formulation) and derivatives (e.g., specific heats, speed of sound, partial properties) can be calculated in a straightforward manner. Note that the pressure and temperature resulting from this single-phase model may correspond to unstable thermodynamic states.

2.3. Multi-component two-phase equilibrium model

A mixture is considered stable at the current temperature and pressure if and only if the total Gibbs energy is at its global minimum (Michelsen and Mollerup, 2007). To account for the possible coexistence of two separate phases, density, internal energy and fluid composition within a finite-volume cell are passed to a thermodynamic solver in which it is tested whether this state corresponds to a point within or outside the two-phase region. Whether a split into two phases yields a decrease in the Gibbs energy, or, in other words, whether the fluid state within a computational cell lies within the two-phase region or not, is determined by the Tangent Plane Distance (*TPD*) function (Michelsen, 1982). Consider a N_c-component mixture with $N_c \geq 2$ of composition $\mathbf{z}$ at a given temperature T and pressure p. For a trial phase composition $\mathbf{w} = \{w_1, \ldots, w_{N_c}\}$, the *TPD* is expressed by

$$TPD(\mathbf{w}) = \sum_{i=1}^{N_c} w_i[\underline{\mu}_i(\mathbf{w}) - \underline{\mu}_i(\mathbf{z})] \tag{20}$$

with $\underline{\mu}_i$ being the chemical potential (which is the partial molar Gibbs energy) of component i. Analytical expressions for the chemical potential can be found in literature, see, e.g., Elliott and Lira (2012) for the PR EOS. Introducing the fugacity coefficient φ_i through

$$\ln\varphi_i = \frac{\underline{\mu}_i - \underline{\mu}_i^{\text{ig}}}{\mathcal{R}T}, \tag{21}$$

Eq. (20) is commonly expressed in a dimensionless form

$$tpd = \frac{TPD}{\mathcal{R}T} = \sum_{i=1}^{N_c} w_i[\ln\varphi_i(\mathbf{w}) + \ln w_i - d_i(\mathbf{z})] \tag{22}$$

with

$$d_i(\mathbf{z}) = \ln\varphi_i(\mathbf{z}) + \ln z_i. \tag{23}$$

The phase of composition $\mathbf{z}$ is considered stable at the specified temperature T and pressure p if and only if

$$tpd(\mathbf{w}) \geq 0 \quad \forall \quad w_i \geq 0 \quad \text{such that} \quad \sum_{i=1}^{N_c} w_i = 1. \tag{24}$$

A widely used approach to solve Eq. (24) is to calculate the stationary points of the *tpd* function, i.e., points where the derivative with respect to all independent variables is equal to zero (Michelsen, 1982). Then, non-negativity at all stationary points proves that the mixture is stable. For comprehensive reviews, alternative formulations and solution methods the interested reader is referred to Michelsen (1982), Firoozabadi (1999) and Michelsen and Mollerup (2007). For the present work, we followed the recommendation of Qiu et al. (2014) and implemented the BFGS-quasi-Newton algorithm (see Hoteit and Firoozabadi, 2006 and references therein). A MATLAB code for the *TPD* test using both the BFGS-quasi-Newton algorithm and the successive substitution method can be found in the library described in Appendix C. If the result of the TPD test tells us that the single-phase mixture is stable, then we apply the cubic EOS in a straightforward manner, see Section 2.2. If it turns out that the mixture is unstable, which means that the fluid would prefer to exist as two phases separated by an interface, then we solve the so-called isochoric-isoenergetic flash problem. Temperature and pressure are iterated until the sum (weighted by the phase fraction) of the liquid-phase and vapor-phase volumes and internal energies within a computational cell corresponds to the overall internal energy and volume that come from the flow solver. The corresponding objective function for the two-phase model is

$$\mathbf{F} = \left\{ \frac{\underline{v}^\star - \underline{v}_{EQ}(T,p,\mathbf{z}^\star)}{\underline{v}^\star}, \frac{\underline{e}^\star - \underline{e}_{EQ}(T,p,\mathbf{z}^\star)}{\underline{e}_{norm}} \right\} \tag{25}$$

with $\underline{e}^\star = \underline{e}_{LES}$, $\underline{v}^\star = \underline{v}_{LES}$ and $\mathbf{z}^\star = \mathbf{z}_{LES}$ being the specific molar internal energy and volume and overall composition in the corresponding cell, respectively.

In the innermost iteration loop, we solve an isothermal-isobaric flash problem (known as TP**n** flash), i.e., we calculate the vapor-liquid phase equilibrium (VLE) at given temperature T, pressure p and overall composition $\mathbf{z}$. The necessary condition of thermodynamic equilibrium is that the chemical potential $\underline{\mu}_i$ of each component i is the same in the liquid (subscript l) and vapor (subscript v) phase, i.e.,

$$\underline{\mu}_{i,v}(T,p,\mathbf{y}) = \underline{\mu}_{i,l}(T,p,\mathbf{x}) \quad \text{for} \quad i = 1,2\ldots N_c. \tag{26}$$

Here and in the following we denote liquid phase mole fractions by $\mathbf{x} = \{x_1 \ldots x_{N_c}\}$ and vapor phase mole fractions by $\mathbf{y} = \{y_1 \ldots y_{N_c}\}$. Typically, Eq. (26) is expanded to

$$F_i = \ln\varphi_{i,v}(T,p,\mathbf{y}) - \ln\varphi_{i,l}(T,p,\mathbf{x}) + \ln K_i = 0 \quad \text{for} \quad i = 1,\ldots,N_c \tag{27}$$

with

$$K_i = \frac{y_i}{x_i} = \frac{\varphi_{i,l}}{\varphi_{i,v}} \tag{28}$$

being the so-called K-factor (or K-ratio or equilibrium factor). The material balance for each component,

$$\underline{\alpha}_v y_i + (1-\underline{\alpha}_v)x_i = z_i, \tag{29}$$

with $\underline{\alpha}_v$ being the overall vapor fraction on a molar basis, and the requirement that mole fractions in the liquid and vapor phase must sum to unity, or equivalently

$$\sum_{i=1}^{N_c} y_i - x_i = 0, \tag{30}$$

yield $(2N_c + 1)$ equations, which are solved for the unknown compositions $\mathbf{x}$ and $\mathbf{y}$ of liquid and vapor, and the molar vapor fraction $\underline{\alpha}_v$. Equilibrium volume $\underline{v}_{EQ}$ and energy $\underline{e}_{EQ}$ in Eq. (25) are then obtained through

$$\underline{v}_{EQ}(T, p, \mathbf{z}^\star) = \underline{\alpha}_v \underline{v}_v + (1 - \underline{\alpha}_v)\underline{v}_l \tag{31}$$

and

$$\underline{e}_{EQ}(T, p, \mathbf{z}^\star) = \underline{\alpha}_v \underline{e}_v + (1 - \underline{\alpha}_v)\underline{e}_l. \tag{32}$$

Liquid phase molar volume $\underline{v}_l(T, p, \mathbf{x})$ and energy $\underline{e}_l(T, p, \mathbf{x})$ and vapor phase molar volume $\underline{v}_v(T, p, \mathbf{y})$ and energy $\underline{e}_v(T, p, \mathbf{y})$ are available as solution to the isothermal flash (which provides liquid phase composition $\mathbf{x} = \{x_1, \ldots, x_{N_c}\}$, vapor phase composition $\mathbf{y} = \{y_1, \ldots, y_{N_c}\}$ and vapor faction $\underline{\alpha}_v$). For a comprehensive review and practical implementation guidelines for the solution of the TP**n** flash the interested reader is referred to the textbook of Michelsen and Mollerup (2007). The algorithm that was used in this work is available as MATLAB source code, see Appendix C.

The outer-loop iteration is done by a multidimensional Newton iteration in T and p. In case of divergence we resort to the robust Trust-Region algorithm that is implemented in Intel's MKL library. The algorithm that was used in this work is given in Algorithm 1 and available as MATLAB source code, see Appendix C. There are a number of noteworthy performance related aspects:

- Available history from previous time steps or Runge-Kutta substeps (superscript $^{n-1}$) for temperature T, pressure p, K-factors K_i, and vapor fraction $\underline{\alpha}_v$ is exploited .
- If the previous thermodynamic state in a computational cell is unknown, we start with a single-phase assumption to obtain (p, T). In Algorithm 1, an unknown state may correspond to a situation where no history is available, e.g., during initialization, or the previous thermodynamic state was stable.
- If the computational cell was in a two-phase state at the previous time- or Runge-Kutta step, we do not evaluate the single-phase thermodynamic model and do not perform the *TPD* test (in the first place). Instead, we assume that the mixture is two-phase and solve the isoenergetic-isochoric flash. If the flash converges to the trivial solution, i.e., $\mathbf{x} = \mathbf{y}$, we evaluate the single-phase thermodynamic model and undertake the *TPD* test. If the mixture turns out to be stable, we are good. This situation represents a computational cell that transitions from a two-phase state to a single-phase state. If the *TPD* test tells us that the mixture is unstable we either solve the isoenergetic-isochoric flash again with a new initial guess for K_i (which now comes from the *TPD* test and not from the previous time step) or just move on. This situation did rarely happen for the cases under consideration.
- If the temperature from the previous time step is above a certain threshold, we assume the mixture to be stable and solve for (p, T) under the single-phase assumption. We used in all subsequent simulations as threshold 1.2 times the critical mixing temperature (which is shown for a binary nitrogen-dodecane mixture at $p = 6$ MPa in Fig. 1) at the corresponding nominal operation pressure.
- We assumed mixtures with any $z_i > 0.9999$ to be stable.

The two latter points significantly reduce the required number *TPD* tests. Note that the last assumption must not be used for single-species two-phase simulations, e.g., in cavitating nozzles of fuel injectors.

2.4. Discretization method and turbulence model

The governing equations of the FC formulation, Eqs. (1)–(4), are discretized by a conservative finite-volume scheme. In general, any stable and consistent LES method could be used. We model effects of unresolved subgrid scales (SGS) by the adaptive local deconvolution method (ALDM) of Hickel et al. (2014). In order to avoid spurious oscillations at sharp density gradients, we additionally apply the van Albada limiter (van Albada et al., 1982) for the reconstruction of mass and internal energy. The flux provided by these methods ensures oscillation-free pressure-velocity coupling through an approximate solution of the compressible Riemann problem that is consistent with incompressible turbulence theory in the low-Mach limit, see Appendix B of Ref. (Hickel et al., 2014). The viscous flux is discretized with a 2nd order central difference scheme. The left-hand side of the pressure-evolution equation for the QC method is discretized consistently with the internal energy transport, such that both discretizations are identical up to machine precision for a single-species perfect gas. The 3rd order explicit Runge-Kutta scheme of Gottlieb and Shu (1998) is used for time integration. The time step size is dynamically adapted such that CFL=1.0, which corresponds for the default grid of the Spray A LES to about 1.7–1.9 ns.

ALDM accurately models the effects of unresolved turbulent transport, SGS dissipation and diffusion through nonlinear local deconvolution and a nonlinear tensor diffusivity (Hickel et al., 2006, 2014) and has been applied and validated for LES of several real-gas injector flows, see Refs. Matheis and Hickel (2016) and Matheis et al. (2016, 2015). The VLE closure can be seen as an SGS model for the effects of unresolved phase interfaces on the filtered pressure and filtered temperature. We believe that these are the most important SGS terms; however, we should also note that there are more terms that our present model does not account for. As highlighted by Selle et al. (2007) and Taşkinoğlu and Bellan (2010), e.g., additional SGS terms appear in the derivation of the LES equations due to the nonlinearity of the EOS and variable transport coefficients and can become important under high-pressure conditions. Models for these unconventional SGS terms, i.e., the filtered pressure, filtered heat flux, and filtered species mass fluxes, have been proposed by Borghesi and Bellan (2015) and others. However, their performance for practical applications at high Reynolds number is yet to be explored. As pointed out by Gnanaskandan and Bellan (2017a, 2017b), higher-order statistics and spatial details from experimental data (or DNS data) are necessary to allow for the validation of such novel SGS models. Because of the limited availability of such data for ECN Spray A, and because the validation of novel SGS models is beyond the scope of this work, we do not explicitly account for these additional SGS terms.

3. Evaluation of the thermodynamic models

To address the accuracy of vapor-liquid equilibria calculated with the PR EOS and the mixing and combining rules introduced in Section 2.2, consider the pressure-composition phase diagram in Fig. 1(a). Bubble-point and dew-point lines are calculated by solving Eq. (26) for the unknown mixture mole fractions in the liquid ($\mathbf{x}$) and vapor ($\mathbf{y}$) phases at given pressure p and temperature T. The nominal Spray A operating pressure of 6 MPa is shown by the dashed horizontal line and six bubble-point and dew-point lines are shown for $344.4\text{K} \leq T \leq 593.5\,\text{K}$. At such high pressures and relevant temperatures a significant amount of the ambient gas, i.e., nitrogen, is dissolved in the fuel-rich liquid phase. While we observe a good prediction of the nitrogen mole fraction in the vapor phase, its liquid phase composition is overestimated in comparison to available experimental data. It is possible to improve the prediction for the nitrogen absorption into the liquid phase by re-

Algorithm 1 Update temperature and pressure using the two-phase model and the fully-conservative formulation of the governing equations.

Input: Density ρ, partial densities ρY_i of species $i = \{1 \dots N_c\}$ and internal energy e; temperature T^{n-1}, pressure p^{n-1}, K-factors $\mathbf{K}^{n-1}$ and molar vapor fraction $\underline{\alpha}_v^{n-1}$ from last time- or RK-step (superscript $^{n-1}$)
Output: T^n, p^n, $\mathbf{K}^n$ and $\underline{\alpha}_v^n$ at current time- or RK-step
Convert input to molar quantities and calculate overall molar composition $\mathbf{z}$
$p^n \leftarrow p^{n-1}$; $T^n \leftarrow T^{n-1}$; $\mathbf{K}^n \leftarrow \mathbf{K}^{n-1}$; $\underline{\alpha}_v^n \leftarrow \underline{\alpha}_v^{n-1}$ // Best guess for solution
if T^n is greater than a certain threshold **then**
  // Speed up your LES and do TPD/VLE only where it is necessary.
  // Threshold could be 1.2 × critical mixing temperature.
  $state^n \leftarrow singlephase$; $mixture \leftarrow stable$
else if any z_i is greater than a certain threshold **then**
  // We assumed mixtures with any z_i greater 0.9999 to be stable.
  $state^n \leftarrow singlephase$; $mixture \leftarrow stable$
else if $state^{n-1} = multiphase$ **then**
  // The cell was in a two-phase state last time step or Runge-Kutta step
  $state^n \leftarrow multiphase$; $mixture \leftarrow \mathbf{not}(stable)$
else
  $state^n \leftarrow unknown$; $mixture \leftarrow stable$
end if
if $state^n = unknown$ **or** $state^n = singlephase$ **then**
  $\{T^n, p^n\} \leftarrow \mathbf{solveSinglephase}(\mathbf{z}, \underline{v}, \underline{e}, T^n, p^n)$ // Compute assumed single-phase solution, see Sec. 2.2
  if $T^n < 0.$ **or** $p^n < 0.$ **then**
    $state^n \leftarrow multiphase$; $mixture \leftarrow \mathbf{not}(stable)$ // There will be no TPD test
    $p^n \leftarrow p^{n-1}$; $T^n \leftarrow T^{n-1}$
    Initialize K-factors $\mathbf{K}^n$ with Wilson correlation and p^{n-1} and T^{n-1}
  end if
end if
if $state^n = unknown$ **then**
  $\{mixture, \mathbf{K}^n\} \leftarrow \mathbf{solveTPD}(\mathbf{z}, T^n, p^n)$ // See Sec. 2.3
end if
if $mixture = stable$ **then**
  $state^n \leftarrow singlephase$
  if the mixture with volume $\underline{v}$ is a liquid **then** $\underline{\alpha}_v^n = 0$ **else** $\underline{\alpha}_v^n = 1$ **end if**
else
  $\{T^n, p^n, \mathbf{x}^n, \mathbf{y}^n, \underline{\alpha}_v^n\} \leftarrow \mathbf{solveIsoenergeticIsochoric}(\mathbf{z}, \underline{e}, \underline{v}, T^n, p^n, \mathbf{K}^n, \underline{\alpha}_v^n)$
  if sum(abs(**x - y**)) is greater than a certain threshold **then**
    // We may have found the trivial solution $\mathbf{y}^n = \mathbf{x}^n$. We used as threshold 1×10^{-6}
    $state^n \leftarrow multiphase$
    $\mathbf{K}^n \leftarrow \mathbf{y}^n / \mathbf{x}^n$ // Element wise division
  else
    $p^n \leftarrow p^{n-1}$; $T^n \leftarrow T^{n-1}$
    $\{T^n, p^n\} \leftarrow \mathbf{solveSinglephase}(\mathbf{z}, \underline{v}, \underline{e}, T^n, p^n)$
    $state^n \leftarrow singlephase$
    if the mixture with volume $\underline{v}$ is a liquid **then** $\underline{\alpha}_v^n = 0$ **else** $\underline{\alpha}_v^n = 1$ **end if**
    $\{mixture, \mathbf{K}^n\} \leftarrow \mathbf{solveTPD}(\mathbf{z}, T^n, p^n)$
    if $mixture$ is $\mathbf{not}(stable)$ **then**
      We did not find the solution and may call solveIsoenergeticIsochoric again
    end if
  end if
end if

calibrating the binary interaction parameter for the PR EOS, see, e.g., Balaji et al. (2011) and Qiu and Reitz (2015).

Fig. 1(b) shows a temperature-composition phase diagram for the nominal operating pressure of 6 MPa. Bubble-point and dew-point line enclose the two-phase region. The solid and dashed lines correspond to the frozen (T_F, single-phase model) and equilibrium (T_E, two-phase model) adiabatic mixing temperature, respectively, which we calculated according to Qiu and Reitz (2015) and references therein. Note that single-phase and two-phase model do of course collapse outside of the two-phase region. For mixture states located within the two-region, we see differences in temperature of about $\sim$48 K at a molar composition $z_{N2} \sim 0.8$ (which is about 11% with reference to T_F) between the two models. In the following we evaluate partial densities of the assumed single-phase and two-phase models along their corresponding mixing line since it gives an impression of the PVT relation seen by the CFD solver (see also Section 5.2, where we discuss LES results that follow closely the equilibrium mixing temperature). Fig. 1(c) and (d) depict the partial overall densities (ρ_i) of component i along the frozen (T_F) and equilibrium (T_E) mixing temperatures. We also show partial densities in the liquid ($\rho_{i,\,l}$ - blue points) and vapor ($\rho_{i,\,v}$ - red points) phase. Taking phase separation into account significantly alters the overall PVT relation within the two-phase region ($z_{N2} \sim 0.12 - 0.91$). For example, for an overall nitrogen mole fraction $z_{N2} \sim 0.49$ the overall n-dodecane density $\rho_{C12H26}(T_E)$ is about 240 kg/m^3 below the density as predicted by the PR EOS in the single-phase approach (which is about 50% with reference to ρ_F). Note that the temperature difference between frozen and equilibrium approach is here ($z_{N2} \sim 0.49$) negligible. It appears that differences in the density prediction are much more severe compared to the temperature difference between the two thermodynamic closures. The liquid phase nitrogen density $\rho_{N2,\,l}$ in Fig. 1(d) gives an

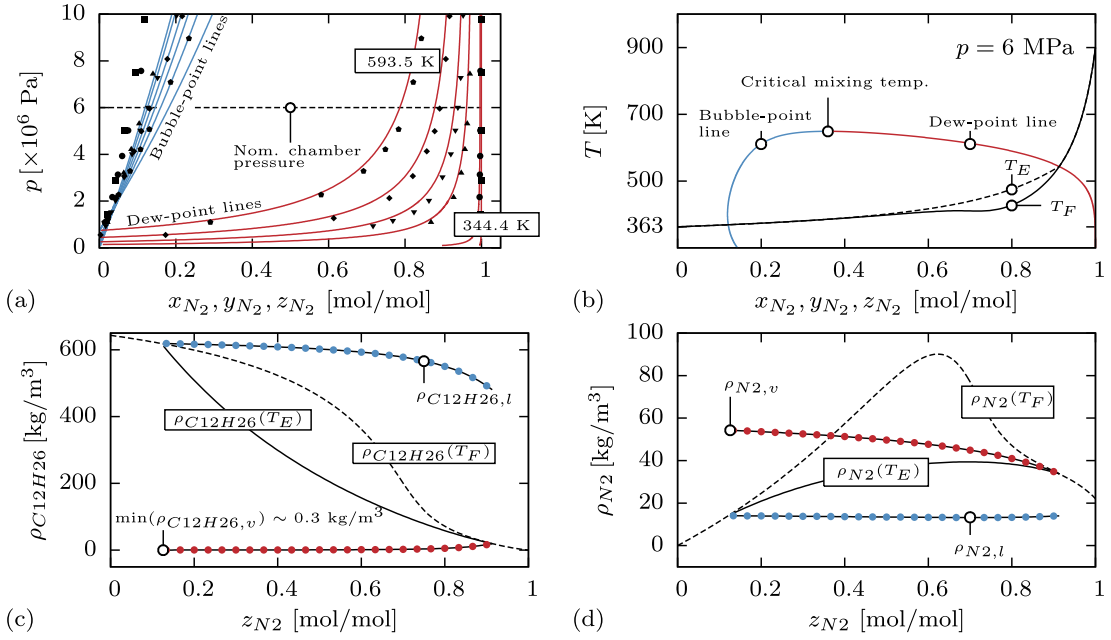

Fig. 1. (a) Pressure-composition phase diagram. Experimental data was provided by DDBST GmbH (2015). (b) Temperature-composition phase diagram at 6 MPa together with frozen (T_F) and equilibrium (T_E) mixing temperature. Dodecane (c) and nitrogen (d) partial overall densities (ρ_i) and partial liquid ($\rho_{i,l}$) and vapor ($\rho_{i,v}$) densities along frozen (T_F) and equilibrium (T_E) mixing temperature. A MATLAB source code (`main_N2_C12H26.m`) that produces the figures (b)-(d) is provided as supplementary material, see Appendix C.

impression on the solubility of nitrogen in the liquid phase where we see a more or less constant value of about 14 kg/m^3. It is also interesting to note that the nitrogen partial density in the vapor phase (and overall nitrogen partial density for $z_{N2} > 0.20$) exceeds its pure component/atmospheric value (~ 22 kg/m^3) up to a factor of ~ 2.45 due to the endothermic process of evaporation and mixing with the fuel vapor (nitrogen is essentially cooled down).

4. Consistency and convergence of FC and QC formulation

Eqs. (1)–(4) (FC) and Eqs. (1)–(3),(5) (QC) are expected to converge to the same solution with increasing grid resolution. To prove this important hypothesis, we show results for a 1-D advection-diffusion test case of a contact discontinuity in Fig. 2. The number of uniform cells in the region of interest ($-l_{ref}/2 < x < l_{ref}/2$) with $l_{ref} = 2 \times 10^{-5}$ m varies from 32 to 2048. Two blocks with stretched cells are attached on both sides, such that reflections from the boundary conditions cannot affect the results.

The chosen thermodynamic conditions are similar to Spray A ($p = 6$ MPa, $T_{N2} = 900$ K, $T_{C12H26} = 363$ K) and the advection velocity is $u = 5$ m/s. Species mass fractions are initialized with an error function profile in physical space

$$Y_{C12H26} = 0.5 - 0.5\ \mathrm{erf}\{(x_i + 0.25 l_{ref})/(0.01 l_{ref})\}, \tag{33}$$

with x_i being the cell-center coordinates. Both FC and QC equations are closed by the single-phase model (FC-F and QC-F). The temperature across the initial interface is computed from a linear enthalpy profile in mixture space, commonly known as the adiabatic mixing temperature.

The first and second columns in Fig. 2 depict the density and velocity at $t = 2 \times 10^{-6}$ s, and the dotted lines represent the initial solution at $t = 0$. The third column shows temperature profiles in mixture space and point symbols along the dotted line visualize the number of grid points across the initial interface. We observe large differences between FC and QC formulations on the coarsest grid, Fig. 2(a)–(c). The FC method shows unphysical velocity oscillations, whereas the QC method yields smooth profiles. Note that physical diffusion causes a change in velocity on the right side of the advected contact discontinuity. The QC method shows much higher temperatures on the n-dodecane side (left) compared to the FC method. With increasing grid resolution, spurious oscillations of the FC method become less severe and eventually disappear, and the temperature profile of the QC method converges towards the FC solution. We conclude from these results that energy-conservation errors – necessary to maintain velocity and pressure equilibria at interfaces without the generation of spurious oscillations – translate into errors in temperature on coarse grids and both methods converge to the same solution on sufficiently fine grids.

5. LES of ECN Spray A

5.1. Grid and boundary conditions

The computational domain is shown in Fig. 3. All simulations have been performed in a rectangular domain with the overall dimensions $L_x = 56$ mm ($\sim 622 D_i$) in the streamwise and $L_y = L_z = 28$ mm ($\sim 311 D_i$) in the lateral directions, where $D_i = 0.09$ mm is the injector diameter. We use an adaptive Cartesian blocking strategy with a static local coarsening/refinement and a varying grid resolution along the spray break-up trajectory to keep computational costs tractable. The grid consists of 2766 blocks with 7 grid-refinement levels and a total number of about 15.1 million cells. Note that the spatial extend of turbulent structures in the near-nozzle region differs significantly from those further downstream. For example, at a streamwise location of $x = 35$ mm, the diameter of the spray cone is roughly 12 mm, which is about 133 times the injection hole diameter. Here, much coarser cells compared to the near-nozzle region are reasonable and necessary given limited computational resources. The smallest cells with $\Delta y_{\min} = \Delta z_{\min} \sim 6.84$ μm and $\Delta x_{\min} = 2\Delta y_{\min}$ are located in the near-nozzle region ($x < 7$ mm), see the zoomed view in Fig. 3. The injector diameter D_i is discretized with about 13 cells. The coarsest cells with

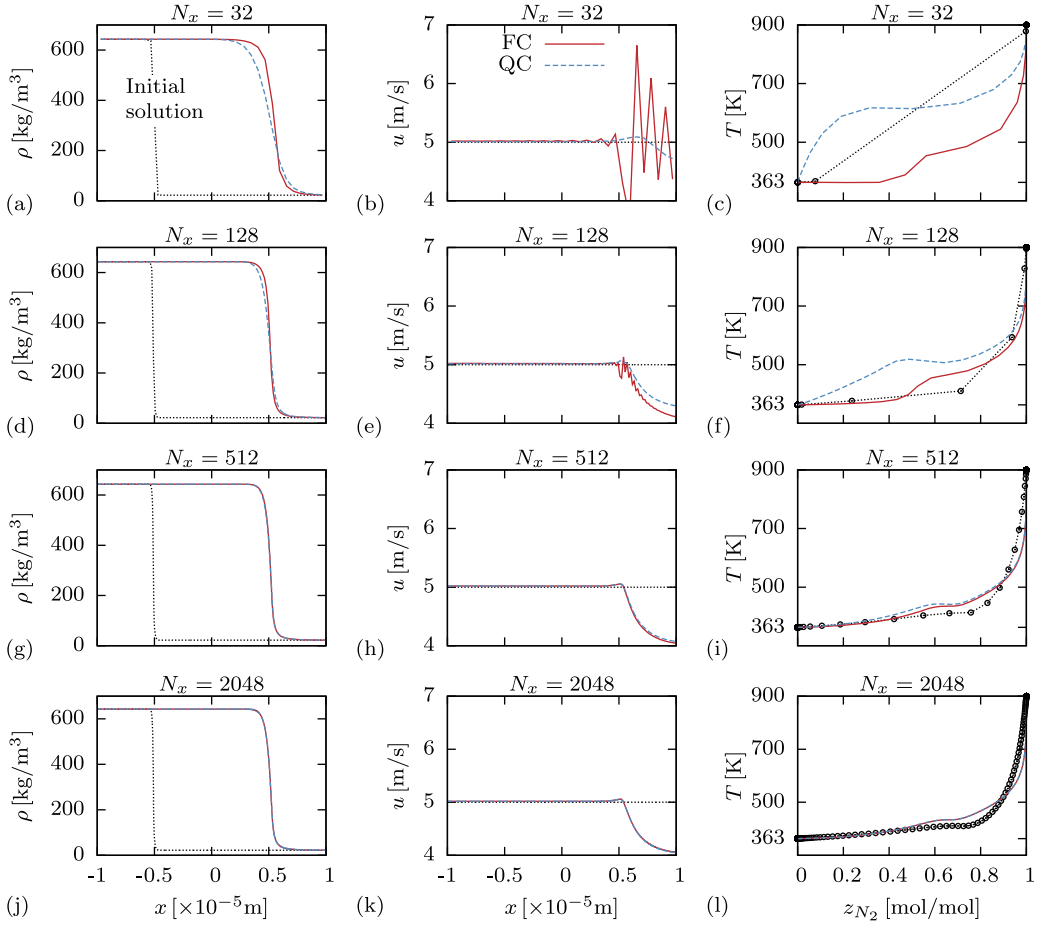

Fig. 2. FC-F and QC-F results for a 1-D advection-diffusion test case for different grid resolutions. Left column: density profiles in physical space; center column: velocity profiles in physical space; right column: temperature profiles in mixture space; dotted lines are the initial profiles.

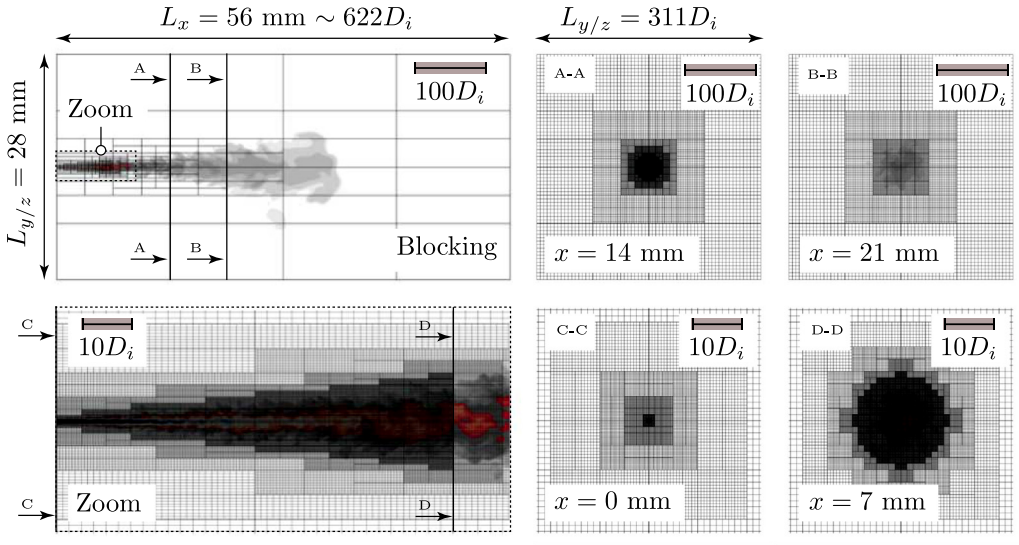

Fig. 3. Blocking and grid resolution ($\mathcal{G}^2$) of the computational domain for LES of Spray A. Note the different scaling factors between top and bottom row.

$\Delta y_{max} = \Delta z_{max} = \Delta y_{min} \times 2^6 \sim 0.44$ mm and $\Delta x_{max} = 2\Delta y_{max}$ are located in regions that are not of interest, e.g., the outer most cells in cut A-A in Fig. 3. The suitability of the grid has been verified by a grid convergence study, see Appendix A.

Fig. 4 depicts the time-dependent velocity and mass flow rate profile that is prescribed for Spray A ($T_A = 900$ K, $p_A = 6$ MPa) simulations. The mass flow rate profile is taken from the CMT website (http://www.cmt.upv.es/ECN03.aspx) with the following input parameters: injection pressure: 150 MPa; outlet diameter: 0.09 mm; fuel density: 703.82 kg/m^3; back pressure: 6 MPa; discharge coefficient: 0.89; injection time: 1.5 ms. The prescribed velocity block profile is calculated from the mass-flow rate with

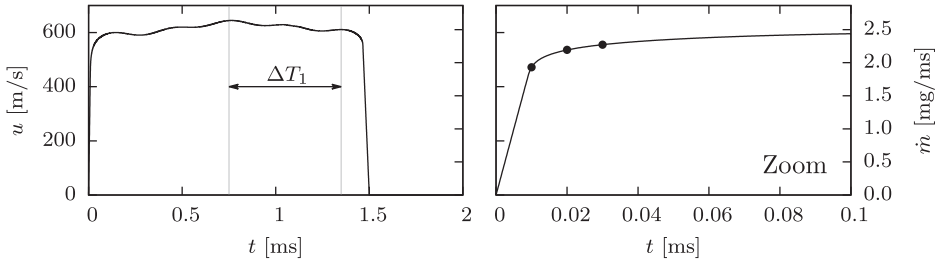

Fig. 4. Injection profile used for LES of Spray A. Left y-axis: Prescribed velocity calculated from mass flow rate with $\rho_{PR}(T = 363\ \text{K}, p = 6\ \text{MPa}) = 643.25\ \text{kg/m}^3$. Right y-axis: prescribed mass flow rate. Points mark time instances shown in Fig. 10.

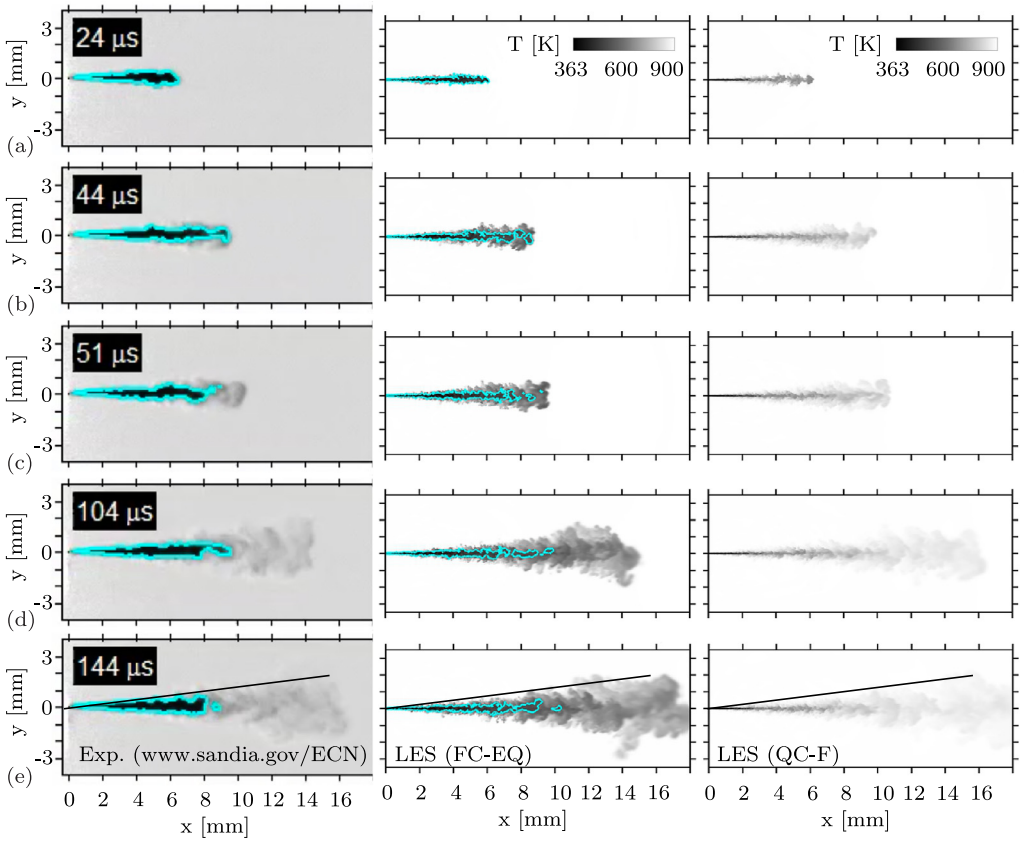

Fig. 5. Temporal sequence of the injection event. Left column: experimental data, see https://ecn.sandia.gov/data/bkldaal1movie/˜and Pickett et al. (2011a) for details; center column: LES with FC-EQ; right column: LES with QC-F. Instantaneous snapshots of the temperature distribution are shown for LES data. Liquid penetration length is illustrated by a $LVF = 0.15\%$ iso-contour.

$\rho_{PR}(T = 363\ \text{K}, p = 6\ \text{MPa}) = 643.25\ \text{kg/m}^3$. The nozzle internal flow is therefore not simulated. We do not introduce any artificial turbulent fluctuations at the inflow patch, since we expect the jet break-up process to be controlled by massive shear forces and high hydrodynamic pressure fluctuations induced by the high-speed jet. At the outlet we prescribe the static pressure of 6 MPa together with a linear extrapolation procedure of all conservative flow variables. All walls are modeled as adiabatic.

5.2. Comparison to experimental data

In the following we use experimental reference data to evaluate our numerical results obtained with the quasi-conservative frozen single-phase model (QC-F) and with the fully conservative equilibrium two-phase model (FC-EQ). The fully conservative single-phase method (FC-F) encountered numerical instabilities during the start-up phase when the jet accelerates from 0 to 600 m/s in just 10 µs. A total time interval of 1.5 ms has been simulated. Fig. 5 depicts a temporal sequence of the early jet evolution (24 µs–104 µs). The left column shows experimental data (diffused back illumination). The center and right columns show snapshots of the temperature distribution for LES with FC-EQ and QC-F methods, respectively. In the case of FC-EQ, the liquid penetration length is illustrated by the cyan isocontour of the liquid volume fraction $LVF = 0.15\%$. We observe a very good qualitative agreement between experimental data and LES with the FC-EQ method. At 24 µs the liquid n-dodecane jet extends about 6 mm into the nitrogen atmosphere; at about 44 µs the liquid length has reached its quasi-steady mean. Later points in time illustrate the vapor evolution. QC-F and FC-EQ simulations predict a very similar vapor penetration trajectory; however, significant differences are observed for the temperature field. The dense n-dodecane jet heats up more quickly and mixing takes place at much higher temperatures with the QC-F model. This effect is not caused by the thermodynamic modeling approach (assumed single-phase vs. two-phase), but rather by energy-conservation errors of the QC method. Fig. 6 shows a

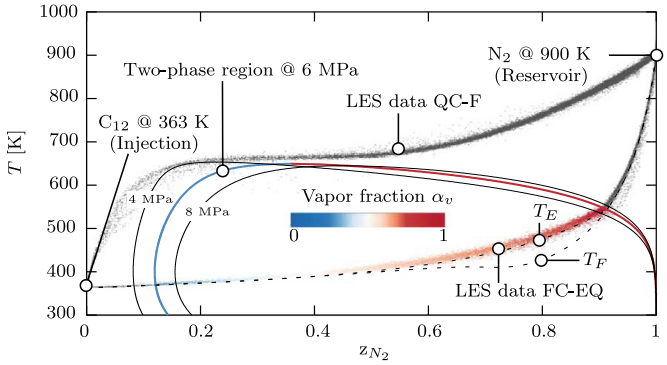

Fig. 6. Temperature-composition diagram for a $N_2 - C_{12}H_{26}$ mixture with frozen (T_F) and equilibrium (T_E) mixing temperature. Scattered data depict the thermodynamic states that are obtained in the QC-F and FC-EQ LES at 144 µs. For FC-EQ, points within the two-phase region are colored by VVF.

temperature-composition phase diagram for the nitrogen-dodecane mixture together with frozen (T_F) and equilibrium (T_E) mixing temperature. The two-phase region is indicated at a pressure of 6 MPa (nominal operating pressure), 4 MPa and 8 MPa. Scattered data depict the thermodynamic states that are obtained in the LES with the methods FC-EQ and QC-F, instantaneous data is taken from Fig. 5(d). In the case of FC-EQ, data points within the two-phase region are colored by the vapor volume fraction (VVF) from blue to red shades. While the FC-EQ LES follows closely the equilibrium mixing temperature, we observe a completely different mixing for the QC-F LES. Above, we demonstrated that the QC solution converges towards the FC solution on fine grids. This means for the LES of Spray A that the QC-F temperature prediction will eventually converge towards the FC solution within the single-phase region when increasing the number of cells and hence reducing the energy conservation error. We therefore conclude that the energy conservation error of the QC method, which translates into an error in temperature, is not controllable for the present application and typical LES grid resolutions. The use of a QC formulation is certainly problematic for flows where a precise temperature prediction is mandatory, such as auto-ignition. Fedkiw et al. (2002) suggested to use the pressure obtained from the pressure-evolution equation only in regions where the interface is numerically problematic. Based on a flow sensor, a non-conservative energy can be calculated from the QC pressure prediction, which locally replaces the energy computed with the FC method. Such an algorithm could improve the energy-conservation properties but is beyond the scope of this paper. In the following we will restrict ourselves to the presentation of LES results that have been obtained with the FC formulation.

A quantitative comparison between experiment and the FC-EQ LES is given in Fig. 7(a) for the liquid and vapor penetration trajectories. In the LES the liquid core length is defined as $L_l = \max\{x(LVF = 0.15\%)\}$, vapor penetration L_v is shown for the definitions $\max\{x(Y_{C12H26} = 1\%)\}$ and $\max\{x(Y_{C12H26} = 0.001\%)\}$. We observe an excellent agreement of L_l with the experimental time-resolved signal. It is important to note that the measured L_l depends on the chosen threshold value. Based on a thorough analysis based on Mie-scatter theory together with assumptions on droplet diameters, Pickett et al. (2011a, 2015) conclude that the *LVF* threshold representing their liquid length is expected to be less than 0.15% at Spray A conditions. The experimental length fluctuates by approximately ± 1 mm about the quasi-steady mean of 10.4 mm; this value is in excellent agreement with our LES data for the threshold value of 0.15%. In order to evaluate the sensitivity on the threshold value, we computed L_l for $LVF = \{3\%, 1\%, 0.15\%, 0.05\%\}$ and obtained $L_l = \{8.83, 9.91, 10.40, 10.49\}$ mm, respectively.

We also observe a good agreement of the vapor penetration trajectory up to approximately 0.6 ms. At later times the penetration depth is slightly overestimated. We expect a systematic over estimation of the vapor penetration due to shortcomings of the PR EOS with respect to the pure n-dodecane density prediction, see Appendix B for a detailed discussion. In the experiment, the vapor penetration length is derived from high-speed schlieren images (according to Refs. Pickett et al. (2009, 2011b) the used system may technically represent a zoomed shadowgraph). We imitate the experimental flow visualization with a numerical schlieren-type image of the axial density gradient $\partial\rho/\partial x$ spatially averaged along the z-direction. Fig. 7(b) and (c) give an impression on how a mixture-fraction threshold compares to a schlieren image. Liquid and vapor boundaries are defined in the same manner as in Fig. 7(a). Numerical and experimental image are strikingly similar. Quantitatively, the vapor penetration depth defined by a 1% mixture fraction threshold seems to slightly underestimate the vapor penetration derived from a schlieren image in the long term evolution.

In Fig. 8 we compare axial (a) and radial (b,c) mixture fraction profiles. Statistical properties have been obtained by averaging LES data in circumferential direction and over a certain time interval (ΔT_1 in Fig. 4). Following the argument of Knudsen et al. (2016),

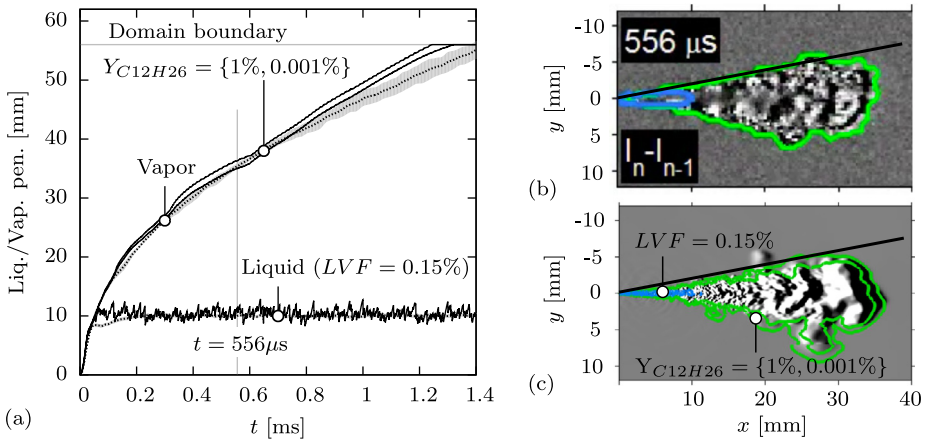

Fig. 7. (a) Numerical (———) and experimental (·····) liquid and vapor penetration trajectories. For LES the liquid core length L_l is defined as $\max\{x(LVF = 0.15\%)\}$, vapor penetration L_v is defined as $\max\{x(Y_{C12H26} = 1\%)\}$ and $\max\{x(Y_{C12H26} = 0.001\%)\}$. (b) Experimental schlieren image. (c) Numerical schlieren image for FC-EQ LES. See Refs. Pickett et al. (2011a,b) and http://www.sandia.gov/ecn/ for details on experimental data (Sandia; Injector SN 210677; 0% O_2; Injection duration 1.5 ms).

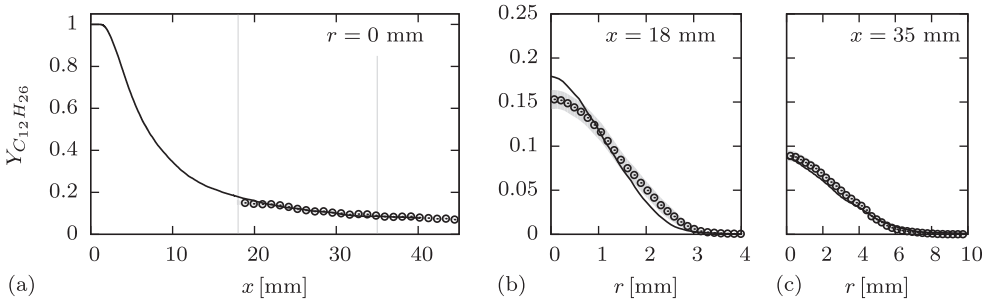

Fig. 8. Axial (a) and radial (b,c) mixture fraction profiles. LES with FC-EQ (———); (⊙) experimental data of Pickett et al. (2011b), see also http://www.sandia.gov/ecn/cvdata/assets/Rayleigh/bkldaAL4mixing.php. Radial profiles are extracted at 18 mm and 35 mm.

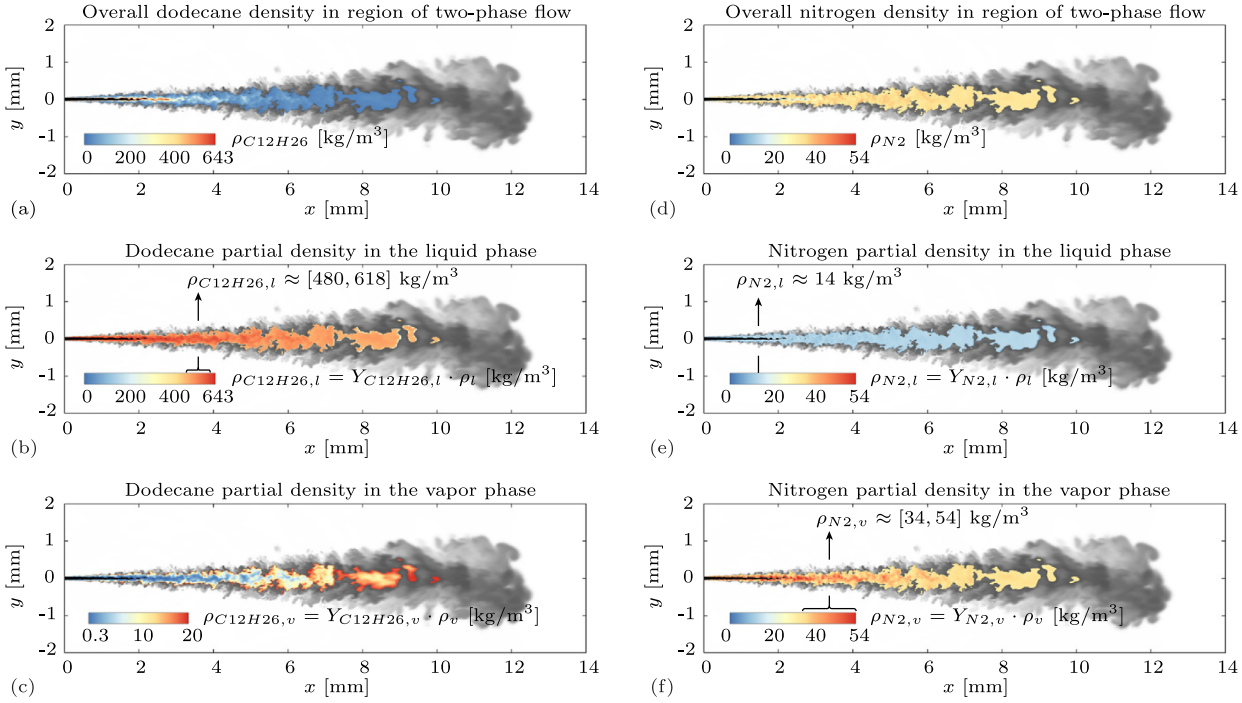

Fig. 9. Full phase information for LES of Spray A using the FC-EQ approach. Left and right column show contours from blue to red shades of dodecane and nitrogen partial densities, respectively. All cells with $0.1\% > VVF > 99.9\%$ are blanked out. The background contour shows the temperature field from dark to light shades. (For interpretation of the references to color in this figure legend, the reader is referred to the web version of this article.)

care must be taken when interpreting these results due to differences in the averaging methods (ensemble averaging vs. time- and circumferential averaging). LES results agree reasonably well with the experimental data. At the $x = 18$ mm station we see an overestimation of the n-dodecane mass fraction on the jet axis. At $x = 35$ mm LES and experimental data collapse.

In the following, we discuss detailed phase information that is readily available through the VLE-based two-phase model. Fig. 9(a) and (b) show contour plots of the overall dodecane and nitrogen partial density or mass concentration

$$\rho_i = Y_i \rho = Y_i[\alpha_v \rho_v + (1 - \alpha_v)\rho_l], \tag{34}$$

where Y_i, ρ_v and ρ_l denote the overall mass fraction of component i, the vapor phase density and the liquid phase density, respectively. All cells with $0.1\% > VVF > 99.9\%$ are blanked out to allow for an isolated view on regions with two-phase flow. This corresponds roughly to regions where $z_{N2} < 0.12$ and $z_{N2} > 0.91$, cf. Fig. 6. The background grayscale contour shows the temperature field, which visualizes the boundaries of the jet. Partial densities of component i in the liquid phase

$$\rho_{i,l} = Y_{i,l}\rho_l \quad \text{with} \quad Y_{i,l} = x_i \frac{M_i}{M_l} \quad \text{and} \quad M_l = \sum_{i=1}^{N_c} x_i M_i \tag{35}$$

are shown in Fig. 9(b) and (e). Partial vapor phase densities

$$\rho_{i,v} = Y_{i,v}\rho_v \quad \text{with} \quad Y_{i,v} = y_i \frac{M_i}{M_v} \quad \text{and} \quad M_v = \sum_{i=1}^{N_c} y_i M_i \tag{36}$$

of each component are given in Fig. 9(c) and (f). $Y_{i,l}$ and $Y_{i,v}$ denote the mass fractions of component i in the liquid and vapor phase; M_v and M_l are the molar masses of the liquid and vapor phases. The different densities shown in Fig. 9 correspond to the analytical solutions of the adiabatic mixing model shown in Fig. 1(c) and (d). The dark region in the very near field of the nozzle marks an intact liquid core of about 2 mm which is essentially pure dodecane in a compressed-liquid state with a density of about 643 kg/m^3. Depending on the local pressure, only a little amount of nitrogen (up to $z_{N2} \approx 0.12$, cf. Fig. 6) can be mixed into liquid dodecane before the formation of a vapor phase must occur. Ambient nitrogen with a density of about $\rho_A(T_A = 900\ K, p_A = 6\ MPa) \approx 22$ kg/m^3 is accelerated by the fuel

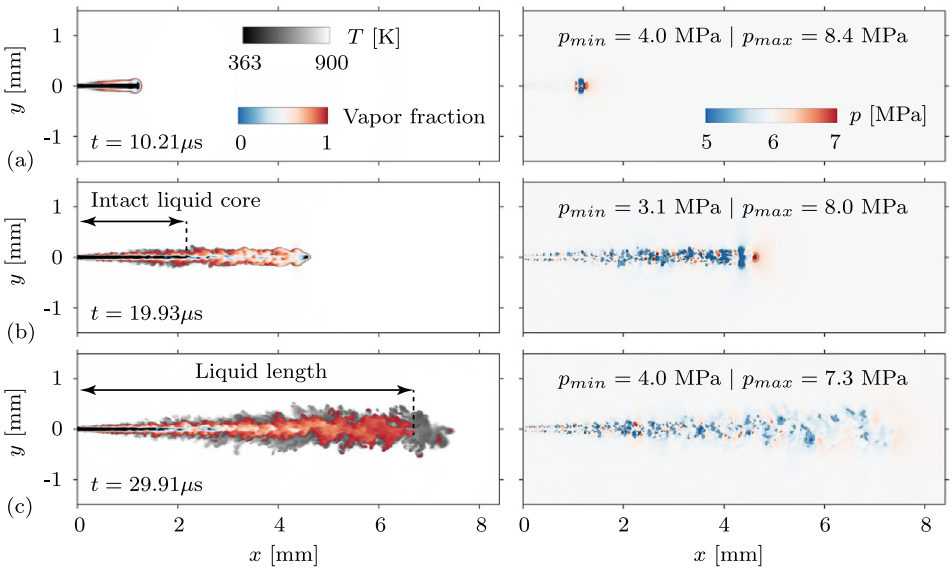

Fig. 10. Temporal sequence of temperature (left) and pressure (right) for FC-EQ LES. Left column: Instantaneous snapshots of the temperature field (contour levels are shown for $363\,\mathrm{K} < T < 900\,\mathrm{K}$, from dark to light shades), superimposed by the VVF distribution (contour levels are shown for $0 < \alpha_v < 1$, from blue to red shades). Right column: Instantaneous snapshots of the pressure field (contour levels are shown for $5\,\mathrm{MPa} < p < 7\,\mathrm{MPa}$, from blue to red shades) together with the maximum and minimum pressure at the corresponding time instance. (For interpretation of the references to color in this figure legend, the reader is referred to the web version of this article.)

jet and mixes into the plume such that the jet becomes a two-phase spray at $x \gtrsim 2$ mm. There, the mass concentration of dodecane in the liquid phase varies depending on mixture temperature and composition between $\rho_{C12H26,\,l} \approx 480\,\mathrm{kg/m^3}$ and $618\,\mathrm{kg/m^3}$, see Fig. 9(b). Because of the high ambient pressure, a significant amount of nitrogen with $\rho_{N2,\,l} \approx 14\mathrm{kg/m^3}$ is dissolved in the liquid phase, see Fig. 9(e). This value occurs to be rather insensitive to local temperature and composition, which can also be seen in Fig. 1(d). Fig. 9(c) depicts the mass concentration of dodecane in the vapor phase, which increases with streamwise distance from $\rho_{C12H26,\,v} \approx 0.3\,\mathrm{kg/m^3}$ to about $20\,\mathrm{kg/m^3}$ (note the different color scaling).

Fig. 10 shows a temporal sequence of the spray structure in the near-nozzle field at a very early state, 10 µs, 20 µs and 30 µs after start of injection. In the left column we show instantaneous snapshots of the temperature field (contour levels are shown for $363\,\mathrm{K} < T < 900\,\mathrm{K}$, dark to light gray shades). Superimposed is the VVF distribution (blue to red shades) for the two-phase region within which the isochoric-isoenergetic flash problem was solved (same coloring as FC-EQ data in Fig. 6). Contours of the corresponding pressure fields ($5\,\mathrm{MPa} < p < 7\,\mathrm{MPa}$, from blue to red shades) are shown in the right column. We see that the n-dodecane-nitrogen mixture locally experiences pressures much different from the average ambient pressure. A region of very low pressure, $p \sim 3$ MPa, can be observed at the tip of the jet due to a start-up vortex ring, see Fig. 10(a) and (b). Just in front of the vortex ring, in the stagnation point of the jet, the pressure exceeds easily 8 MPa. Due to this high pressure, the mixture is here locally in a single-phase state. Even in the fully developed steady state, we see pressure fluctuations in the shear layer in the order of ± 1 MPa. We note that the QC-F method yields a pressure field during ramp-up extremely similar to the FC-EQ results. This supports the conclusion that the reported pressure fluctuations are of physical origin and not caused by the interplay of numerics and nonlinear EOS. We mentioned above that we were not able to simulate Spray A with a conservative single-phase model (FC-F). The instabilities encountered are caused by the single-phase thermodynamics model, which yields ill-defined states at low pressures that occur in well-resolved vortex cores. Our fully conservative two-phase LES model (FC-EQ) did not face any stability problems because the more sophisticated model can resolve multi-component subcritical two-phase states, thus avoiding unphysical states. The QC-F LES based on the pressure evolution equation did not encounter any instabilities since mixing takes place at much higher temperatures, thus avoiding unphysical states within the two-phase region.

Table 2
Test case definition. [a] Nominal experimental operating conditions according to Manin et al. (2012). [b] Calculated using the PR EOS; pure nitrogen atmosphere in the LES. [c] From the NIST Lemmon et al. (2013) at p_A and $T_F = 363$ K. [d] Calculated using the PR EOS at p_A and $T_F = 363$ K.

Case	T_A [K]	p_A [MPa]	ρ_A [kg/m^3]	ρ_F [kg/m^3]
#1	1200[a]	8.00	22.8[a]/22.04[b]	705.79[c]/645.14[d]
#2	900[a]	6.00	22.8[a]/22.06[b]	703.82[c]/643.25[d]
#3	700[a]	4.60	22.8[a]/21.80[b]	702.40[c]/641.86[d]
#4	900[a]	2.04	7.6[a]/7.59[b]	699.74[c]/639.16[d]

6. Parametric variation of the test conditions

In addition to the baseline case Spray A, we evaluate the two-phase equilibrium model for three other operating conditions, which are given in Table 2. Case #1 and Case #3 have nominal the same ambient density as Spray A (Case #2, $\rho_A = 22.8$ kg/m^3) but differ in ambient pressure and temperature. Case #4 has a much lower nominal ambient density of $\rho_A = 7.6$ kg/m^3 and the same nominal ambient temperature as Spray A ($T_A = 900$ K). We compare LES-data with diffused back illumination (DBI) data (https://ecn.sandia.gov/dbi675/) and quasi-steady liquid-length measurements (Manin et al., 2012). All simulations in the following section are conducted with the fully conservative two-phase LES model. The computational domain is the same as described in Section 5.1 for the Cases #1 and #2. To ensure the same grid resolution in regions with two-phase flow, $x < L_l$, we adjusted the grid coarsening levels for the Cases #3 and #4. The $\times$ symbols on the y-axis in Fig. 12 mark the axial position at which the grid is coarsened by a factor of 2. As it can be seen, the two-phase region does not exceed the 3rd grid-coarsening level for all cases under consideration. The mass flow rate profile is taken from the CMT

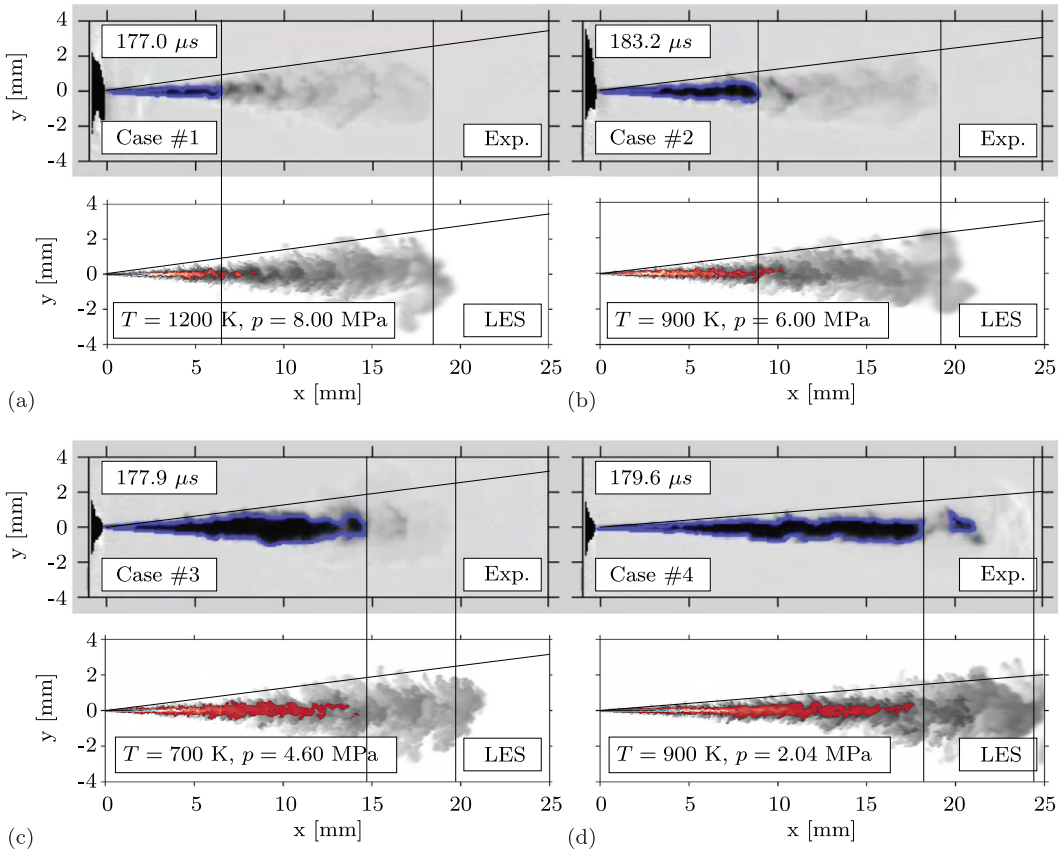

Fig. 11. Comparison between experimental diffused back illumination (DBI) images (https://ecn.sandia.gov/dbi675/, see also Manin et al. (2012)) and instantaneous LES snapshots of the temperature field (contour levels are shown for $363\,\mathrm{K} < T < T_A$, from dark to light shades), superimposed by the VVF distribution (contour levels are shown for $0 < \alpha_v < 1$, from blue to red shades). (For interpretation of the references to color in this figure legend, the reader is referred to the web version of this article.)

website (http://www.cmt.upv.es/ECN03.aspx). Back pressure p_A, n-dodecane density ρ_F (NIST Lemmon et al., 2013) and the density of the nitrogen atmosphere for the different operating points are summarized Table 2. Inflow boundary conditions are then defined in the same manner as for the LES of Spray A, see Section 5.1. A total time interval of 0.5 ms has been simulated, which is sufficient to obtain the quasi-steady liquid length.

Fig. 11 depicts a qualitative comparison between experimental DBI images (https://ecn.sandia.gov/dbi675/) and instantaneous LES snapshots of the temperature field (contour levels are shown for $363\,\mathrm{K} < T < T_A$, from dark to light shades), superimposed by the VVF distribution (contour levels are shown for $0 < \alpha_v < 1$, from blue to red shades). Solid lines indicate roughly the liquid and vapor penetration lengths as well as the spreading angle of the spray obtained from the experimental DBI snapshot. Fig. 11(a)–(c) illustrate the effect of decreasing the ambient temperature from $T_A = 1200\,\mathrm{K}$ to $T_A = 900\,\mathrm{K}$ and $T_A = 700\,\mathrm{K}$ at nominal constant ambient density $\rho_A = 22.8\ \mathrm{kg/m^3}$. Qualitatively, the trend of an increasing liquid penetration length, caused by a decreased evaporation rate at lower temperature, is well reproduced in the LES. We also see that the dark region, which represents roughly the liquid phase in the experiment, spreads in radial direction with decreasing temperature. A similar observation can be made for the colored two-phase region. The penetration depth of the more diffusive region that represents vaporized fuel does not differ much between the three cases due to the same nominal ambient density. As discussed in Appendix B, we see a minor systematic overestimation of the tip penetration in the LES for all cases under consideration. Fig. 11(d) compares the DBI and LES snapshot at a much lower ambient density of $\rho_A = 7.6\ \mathrm{kg/m^3}$. We observe a longer liquid core, an increased penetration depth of vaporized fuel and a smaller spray spreading angle compared to the baseline case. Qualitatively, LES and DBI image share these characteristics, however, the liquid penetration length appears to be slightly underestimated in the LES (see Appendix B for a possible explanation).

In Fig. 12 we compare quantitatively experimental (for references see caption of Fig. 12) and numerical liquid-penetration trajectories. Again, in the LES the liquid-core length is defined as $L_l = \max\{x(LVF = 0.15\%)\}$. In the experiment the liquid penetration length is derived from DBI images based on a threshold criterion quantifying the loss of light through the spray. For a thorough discussion we refer to Manin et al. (2012) and Pickett et al. (2015, 2011a).

In panel (b) of Fig. 12, baseline case Spray A (Case #2), we included also liquid penetration data from another injector. Nominally all injectors share the same specifications; however, each individual injector is slightly different due to manufacturing accuracies. The differences between the two data sets may thus serve as an estimate for the experimental uncertainties. We see a very good prediction of the time-resolved signal for the 1200 K (Case #1) and 900 K (Case #2) atmosphere and a good prediction for the 700 K (Case #3) atmosphere and the low-density atmosphere (Case #4). Interestingly, all experimental data show a longer initial transient until a quasi-steady liquid length is established in comparison to our LES results, most prominent for Case #4 where the quasi-steady liquid penetration is reached only for $t > 0.5$ ms. LES data show an initial transient of $t < 0.1$ ms. These differences are expected to stem from uncertainties in the individual inflow boundary conditions used in the LES, which do not include turbulence and wave dynamics within the injector.

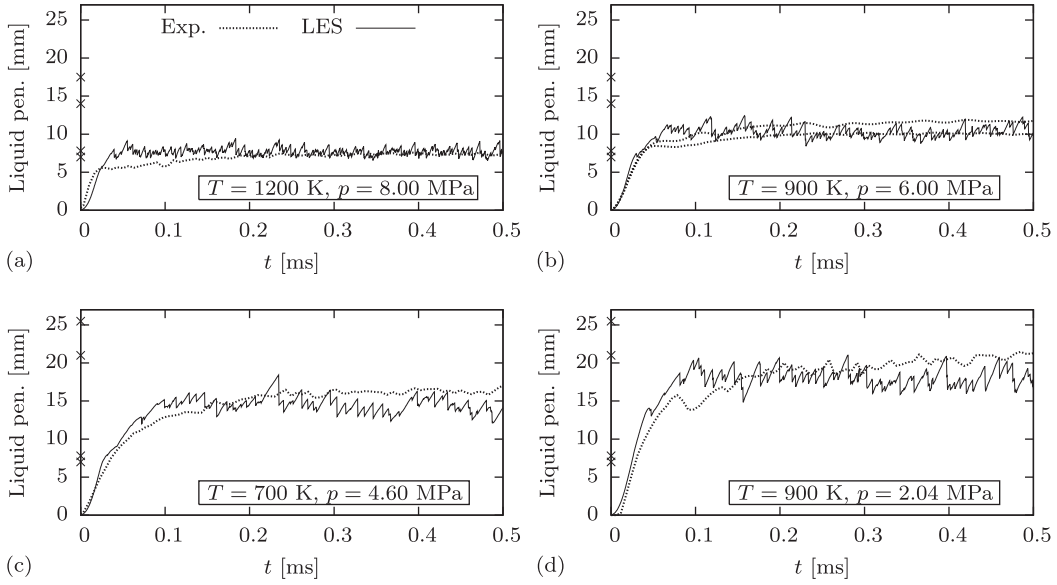

Fig. 12. Numerical (———) and experimental (·····) liquid penetration trajectories for Cases #1–#4. For LES the liquid core length L_l is defined as $\max\{x(LVF = 0.15\%)\}$. See Manin et al. (2012) and https://ecn.sandia.gov/dbi675/ for details on experimental data (Sandia; Injector SN 210675; 0% O_2; Injection duration 1.5 ms). In panel (b), baseline Spray A (Case #2), we show also liquid penetration data from Injector SN 210677, cf. Fig. 7(a).

In conclusion, we found an overall good qualitative and quantitative agreement between experiment and LES for all four operating points, demonstrating the excellent predictive performance of the present methodology for LES of high-pressure high-temperature fuel injection processes.

7. Discussion and concluding remarks

A two-phase model for the Eulerian large-eddy simulation (LES) of turbulent mixing at high pressures has been presented and applied for liquid-fuel injection under four different high-pressure operating conditions. The thermodynamics model is based on cubic equations of state (EOS) and vapor-liquid equilibrium (VLE) calculations. It can thus accurately represent supercritical states as well as coexisting multi-component subcritical two-phase states. The model accounts for fuel compressibility and effects associated with real-fluid thermodynamics, such as the solubility of ambient gas into the liquid phase or variable thermo-physical properties. Our approach yields a thermodynamically consistent and tuning-parameter-free framework for accurate, predictive LES at tractable computational cost. It provides detailed phase information without any semi-empirical break-up and evaporation models; the only input parameters required are the NASA polynomials, the critical properties, and the acentric factor of each species, and if available the binary interaction parameter.

In this paper, we have demonstrated the computational feasibility and accuracy of LES with VLE thermodynamics based on cubic EOS for the ECN Spray A baseline case and three additional operating conditions. Our LES results demonstrated the excellent predictive performance of the VLE model combined with a mass, momentum and energy conserving numerical method. The predicted liquid volume fraction, for example, provides a non-arbitrary definition of the liquid penetration length that can be linked to experimental measurements. Grid convergence of liquid and vapor penetration trajectories has been proven for the baseline case ECN Spray A.

We saw that the Spray A n-dodecane-nitrogen mixture locally experiences pressures significantly below the nominal operating pressure of 6 MPa when the jet accelerates from 0 to 600 m/s in just 10 µs. For these harsh conditions, LES with a conservative dense-gas single-phase approach may encounter unphysical thermodynamic states and the results may thus exhibit large spurious pressure oscillations that can cause numerical instability even with low-order upwind numerics. It has been suggested previously that stable time integration of single-phase thermodynamic models can be obtained by "'energy-correction methods" that sacrifice energy conservation in some way. We therefore compared a fully conservative formulation of the governing equations with a quasi-conservative formulation based on a pressure-evolution equation. We proved (for on a one-dimensional multi-component advection-diffusion test case) the physical and numerical consistency of both methods and convergence towards the same solution for sufficiently fine grids if a small and usually neglected term is included. On coarser grids, however, energy conservation errors associated with the quasi-conservative formulation were much larger than anticipated based on previously published results for other cases and caused a significant overestimation of the temperature.

LES with the fully conservative VLE-based homogeneous two-phase mixture model did not show any stability problems for all test conditions and yielded numerical predictions that are in very good agreement with available experimental data. We therefore conclude that the representation of multi-component subcritical two-phase states is necessary for a stable and physically meaningful Eulerian LES with real-fluid EOS for the cases under consideration. Potential applications of this model are high-pressure injection flows in liquid rocket engines, modern diesel engines and gas turbines.

Typically, two-phase flows are divided into dense, moderately dense, and dilute regimes. In sprays, all of these regimes are present. The assumptions underlying our model hold for dense and moderately dense high-pressure injection cases with typically high Weber number and low Stokes number, such as Spray A, where the droplet diameters are small and surface tension is low. In such application the droplet vaporization time scale and the droplet inertial time scales are sufficiently small, that is, much smaller than the hydrodynamic time scales and of the order of the computational time step. However, in the case of a dilute spray with large Stokes number (large droplets, very small liquid volume fraction, particle-particle interactions are rare) the Eulerian continuum assumption with a single-valued velocity for both phases is

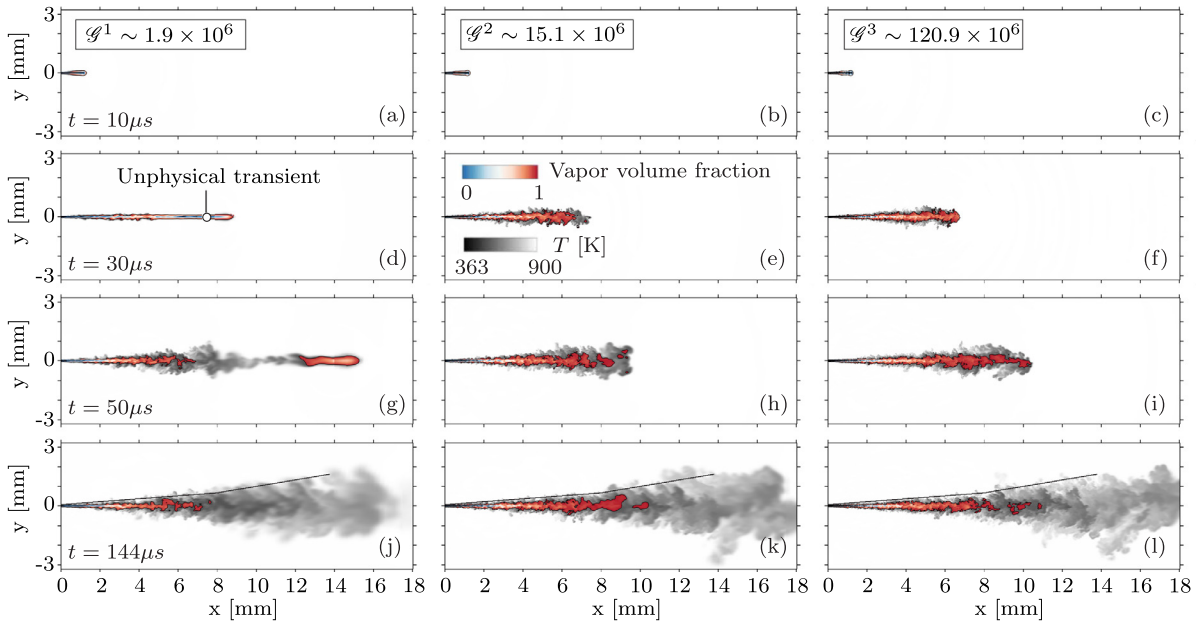

Fig. A.13. Temporal sequence of the injection event at different grid refinement levels $\mathcal{G}^1$ (left), $\mathcal{G}^2$ (center), and $\mathcal{G}^3$ (right). Instantaneous snapshots of the temperature field (contour levels are shown for $363\,\mathrm{K} < T < 900\,\mathrm{K}$, from dark to light shades), superimposed by the VVF distribution (contour levels are shown for $0 < \alpha_v < 1$, from blue to red shades) are shown. (For interpretation of the references to color in this figure legend, the reader is referred to the web version of this article.)

essentially invalid. We therefore expect to see limitations of the homogeneous-mixture approach if the spatial extend of such dilute regions is large compared to moderately dense and very dense regions and if there is a significant slip velocity between a dispersed liquid and gas phase. In such cases, a coupling between the Eulerian VLE-based two-phase model for the primary jet breakup and a Lagrangian spray solver may improve the predictive performance of the simulation.

Future work should also characterize the sensitivity of integral flow properties, such as liquid and vapor penetration trajectories, with respect to the EOS model, the binary interaction parameter and inflow boundary conditions (e.g., nozzle internal flow, velocity profile, synthetic turbulence). We see a large potential for LES that capture the coupling between internal nozzle flow and jet breakup. Because flash boiling and cavitation can be handled with cubic EOS in the VLE-based framework, see, e.g., Star et al. (2006), the full simulation of a gasoline or diesel injection cycle including needle movement – as it was done by Örley et al. (2017) – is feasible. In this paper, only binary systems were studied; however, the application of the VLE-based closure to multi-component two-phase systems is possible without any further modification.

Acknowledgments

This work would not have been possible without the long-term cooperation with Hagen Müller and Michael Pfitzner from the Bundeswehr University Munich. Part of this research has been performed during the 2016 Summer Program of the Center for Turbulence Research (CTR) at Stanford University; we thank the CTR for hospitality and financial support. We are grateful to Chao Ma, Daniel Banuti, Lluis Jofre, Matthias Ihme and Laurent Selle for valuable discussions during the Summer Program. This project was funded by the German Research Foundation (DFG) through the SFB/Transregio 40 and the TUM Graduate School. The authors gratefully acknowledge the Gauss Centre for Supercomputing e.V. (www.gauss-centre.eu) for providing computing time (and a hands-on system-support) on the GCS Supercomputer SuperMUC at Leibniz Supercomputing Centre (www.lrz.de). Last but not least, we thank Lyle Pickett (Sandia National Laboratories) for giving us the permission to use experimental data from the Engine Combustion Network (ECN).

Appendix A. Grid convergence study

To assess the quality of the LES results we present a grid convergence study for which we uniformly refined ($\mathcal{G}^3$) and coarsened ($\mathcal{G}^1$) the base grid ($\mathcal{G}^2$) by a factor of 2. For the highest ($\mathcal{G}^3$) and lowest ($\mathcal{G}^1$) grid resolution we obtain a total number of about 1.89×10^6 and about 120.9×10^6 computational cells, respectively. For reasons discussed in Section 5.2, the grid convergence study is conducted only for the FC set of governing equations together with the two-phase model. Fig. A.13 shows a temporal sequence of the injection event at different grid refinement levels $\mathcal{G}^1$ (left), $\mathcal{G}^2$ (center), and $\mathcal{G}^3$ (right). Instantaneous snapshots of the temperature field (contour levels are shown for $363\,\mathrm{K} < T < 900\,\mathrm{K}$, from dark to light shades), superimposed by the VVF distribution (contour levels are shown for $0 < \alpha_v < 1$, from blue to red shades) are shown. While $\mathcal{G}^2$ and $\mathcal{G}^3$ yield qualitatively a very similar jet break-up phenomenology and subsequent vapor penetration trajectory, we observe on the coarsest grid $\mathcal{G}^1$ a different and unphysical transient. Shear layer instabilities, which lead to a spreading and turbulent mixing in radial direction, start to develop at a later point in time after start of injection. As a consequence, we see a pocket of dense fluid traveling ahead of the spray tip, see Fig. A.13(g). Knudsen et al. (2016) observed the same phenomenon on their coarsest grid. They concluded precisely that an “insufficient transfer of momentum to the radial direction leaves an oversupply of axial momentum that convects the fuel vapor downstream too rapidly”.

Fig. A.14 shows a comparison of liquid and vapor penetration trajectories. Again, grid level $\mathcal{G}^2$ and $\mathcal{G}^3$ yield very similar liquid and vapor penetration trajectories. Slight differences can be observed when the liquid phase transitions to its quasi-steady mean (compare also Fig. A.13(h) and (i)). The coarsest grid $\mathcal{G}^1$ shows a significant overestimation of the initial liquid phase penetration which then abruptly drops to its quasi-steady mean once all the liquid which was convected downstream too rapidly is vaporized. The offset in the vapor penetration persists for the time interval under consideration. For the time-averaged liquid length

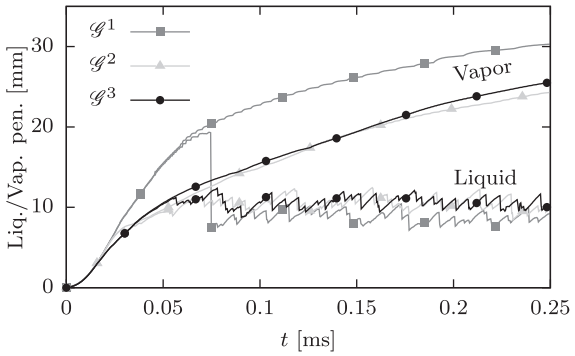

Fig. A.14. Numerical liquid and vapor penetration trajectories for different grid refinement levels $\mathcal{G}^1$, $\mathcal{G}^2$ and $\mathcal{G}^3$. The liquid core length L_l is defined as $\max\{x(LVF = 0.15\%)\}$, vapor penetration L_v is defined as $\max\{x(Y_{C12H26} = 1\%)\}$.

($0.10\,\text{ms} \leq t \leq 0.25\,\text{ms}$) we obtain 8.81 mm ($\mathcal{G}^1$), 10.51 mm ($\mathcal{G}^2$) and 10.65 mm ($\mathcal{G}^3$) along the different grid refinement levels. Given the negligible differences between base grid $\mathcal{G}^2$ and refined grid $\mathcal{G}^3$ (but significant differences with respect to computational time and resources) we used only the base grid $\mathcal{G}^2$ in all simulations.

Appendix B. Accuracy of the Peng–Robinson EOS

Fig. B.15 shows the density, specific heat capacity at constant pressure, speed of sound and dynamic viscosity prediction as function of temperature for pure n-dodecane at a pressure of 6 MPa for different cubic EOS models. Reference data is taken from the NIST (Lemmon et al., 2013). The gray line indicates the n-dodecane injection temperature of 363 K. It is worth noting that popular EOS such as the PR EOS and Soave-Redlich-Kwong (SRK) EOS are not able to accurately reproduce the density of the NIST reference data at temperatures that are typical for injection systems, see Fig. B.15(a). The same is true for other hydrocarbons (Kim et al., 2012). For the operating conditions of Spray A, the error in density prediction of the PR EOS compared to the NIST reference data is about 8.6%. To match the mass-flow measurement, it is necessary to increase the injection velocity, thus, the error in density prediction leads to an error in velocity of about 50 m/s. We checked the sensitivity of vapor penetration trajectories (i.e., vapor penetration over time) to uncertainties resulting from the EOS model, i.e., fuel density ρ_F, ambient gas density ρ_A and inflow velocity, with the *uniform-profile model* of Naber and Siebers (1996). As a result we must expect a slight but systematic overestimation of the vapor penetration by about 3% at Spray A conditions in the LES. The same holds for the liquid length L_l where we may face – according to the *liquid length scaling law* of Siebers (1999) (Eq. 18b, $L_l \propto \sqrt{\rho_F/\rho_A}$) – a systematic underestimation of about 2% for the Cases #1–3 and 4% for Case #4 (see Table 2 for the operating point description).

The accuracy of the PR EOS could be improved by volume translation methods; however, we refrain from applying such methods in the VLE framework because of additional computational costs and possible thermodynamic inconsistencies (Matheis et al., 2016). As indicated in Fig. B.15(a), a new and promising candidate to improve liquid densities of hydrocarbons while maintaining the sim-

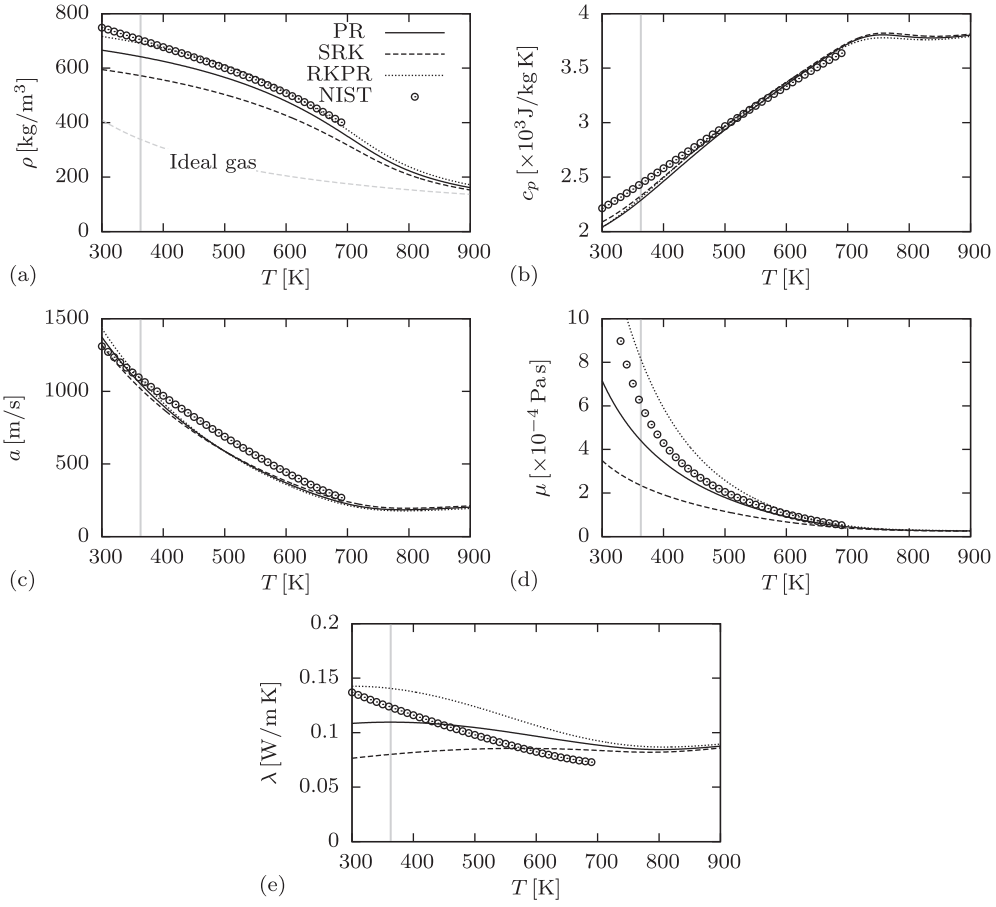

Fig. B.15. Density (a), specific heat capacity at constant pressure (b), speed of sound (c), dynamic viscosity (d), and thermal conductivity (e) prediction for pure n-dodecane at a pressure of 6 MPa for different cubic EOS models, see panel (a) for the line legend. Reference data is taken from the NIST (Lemmon et al., 2013). The gray line indicates the n-dodecane injection temperature of 363 K.

plicity of the framework associated with cubic EOS is the generalized Redlich-Kwong-Peng-Robinson (RKPR) EOS (Cismondi and Mollerup (2005), see also the comprehensive paper of Kim et al. (2012)).

Appendix C. MATLAB Source Code

A collection of MATLAB scripts as supplementary material is available under https://www.gitlab.com/jmatheis/LibThermo. The repository contains a number of scripts that can be used to compute and plot some of the figures presented in this paper. These scripts use elementary functions such as the *TPD* stability analysis or the isothermal two-phase flash. Thermodynamic routines in the Fortran written CFD code INCA (http://www.inca-cfd.com/) that was used for all simulations are based upon these MATLAB scripts. Detailed comments and relevant literature are provided within each individual MATLAB file.

References

Abgrall, R., Karni, S., 2001. Computations of compressible multifluids. J. Comput. Phys. 169 (2), 594–623. doi:10.1006/jcph.2000.6685.

van Albada, G.D., van Leer, B., Roberts Jr, W.W., 1982. A comparative study of computational methods in cosmic gas dynamics. Astron. Astrophys. 108, 76–84. doi:10.1007/978-3-642-60543-7_6.

Balaji, B., Raghavan, V., Ramamurthi, K., Gogos, G., 2011. A numerical study of evaporation characteristics of spherical n-dodecane droplets in high pressure nitrogen environment. Phys. Fluids 23 (6), 063601. doi:10.1063/1.3599700.

Borghesi, G., Bellan, J., 2015. A priori and a posteriori investigations for developing large eddy simulations of multi-species turbulent mixing under high-pressure conditions. Phys. Fluids 27 (3). doi:10.1063/1.4916284.

Chung, T.H., Ajlan, M., Lee, L.L., Starling, K.E., 1988. Generalized multiparameter correlation for nonpolar and polar fluid transport properties. Ind. Eng. Chem. Res. 27 (4), 671–679. doi:10.1021/ie00076a024.

Cismondi, M., Mollerup, J., 2005. Development and application of a three-parameter RK–PR equation of state. Fluid Phase Equilibr. 232 (1), 74–89. doi:10.1016/j.fluid.2005.03.020.

Crua, C., Manin, J., Pickett, L.M., 2015. Transition from droplet evaporation to miscible mixing at diesel engine conditions. In: ICLASS 2015, 13th Triennial International Conference on Liquid Atomization and Spray Systems, Tainan, Taiwan.

Crua, C., Manin, J., Pickett, L.M., 2017. On the transcritical mixing of fuels at diesel engine conditions. Fuel 208, 535–548. doi:10.1016/j.fuel.2017.06.091.

Dahms, R.N., Manin, J., Pickett, L.M., Oefelein, J.C., 2013. Understanding high-pressure gas-liquid interface phenomena in diesel engines. P. Combust. Inst. 34 (1), 1667–1675. doi:10.1016/j.proci.2012.06.169.

Dahms, R.N., Oefelein, J.C., 2013. On the transition between two-phase and single-phase interface dynamics in multicomponent fluids at supercritical pressures. Phys. Fluids 25 (9), 092103. doi:10.1063/1.4820346.

Elliott, J.R., Lira, C.T., 2012. Introductory Chemical Engineering Thermodynamics. Prentice Hall.

Fedkiw, R.P., Liu, X.-D., Osher, S., 2002. A general technique for eliminating spurious oscillations in conservative schemes for multiphase and multispecies euler equations. Int. J. Nonlin. Sci. Num. 3 (2), 99–105. doi:10.1515/IJNSNS.2002.3.2.99.

Firoozabadi, A., 1999. Thermodynamics of Hydrocarbon Reservoirs. McGraw-Hill.

Gnanaskandan, A., Bellan, J., 2017. Large Eddy Simulations of high pressure jets: effect of subgrid scale modeling. In: 55th AIAA Aerospace Sciences Meeting, Grapevine, Texas. American Institute of Aeronautics and Astronautics doi:10.2514/6.2017-1105.

Gnanaskandan, A., Bellan, J., 2017. Numerical simulation of jet injection and species mixing under high-pressure conditions. J. Phys. 821, 012020. doi:10.1088/1742-6596/821/1/012020.

Goos, E., Burcat, A., Ruscic, B., 2009. Third millennium ideal gas and condensed phase thermochemical database for combustion.

Gottlieb, S., Shu, C., 1998. Total variation diminishing Runge–Kutta schemes. Math. Comput. 67 (221), 73–85. doi:10.1090/S0025-5718-98-00913-2.

Hakim, L., Lacaze, G., Oefelein, J.C., 2016. Large eddy simulation of autoignition transients in a model diesel injector configuration. SAE Int. J. Fuels Lubr. 9 (1), 165–176. doi:10.4271/2016-01-0872.

Hickel, S., Adams, N.A., Domaradzki, J.A., 2006. An adaptive local deconvolution method for implicit LES. J. Comput. Phys. 213 (1), 413–436. doi:10.1016/j.jcp.2005.08.017.

Hickel, S., Egerer, C.P., Larsson, J., 2014. Subgrid-scale modeling for implicit large eddy simulation of compressible flows and shock-turbulence interaction. Phys. Fluids 26 (10), 106101. doi:10.1063/1.4898641.

Hoteit, H., Firoozabadi, A., 2006. Simple phase stability-testing algorithm in the reduction method. AIChE J. 52 (8), 2909–2920. doi:10.1002/aic.10908.

Jangi, M., Solsjo, R., Johansson, B., Bai, X.-S., 2015. On large eddy simulation of diesel spray for internal combustion engines. Int. J. Heat Fluid Flow 53, 68–80. doi:10.1016/j.ijheatfluidflow.2015.02.002.

Kim, S.-K., Choi, H.-S., Kim, Y., 2012. Thermodynamic modeling based on a generalized cubic equation of state for kerosene/LOx rocket combustion. Combust. Flame 159 (3), 1351–1365. doi:10.1016/j.combustflame.2011.10.008.

Knudsen, E., Doran, E.M., Mittal, V., Meng, J., Spurlock, W., 2016. Compressible Eulerian needle-to-target large eddy simulations of a diesel fuel injector. P. Combust. Inst. 32 (2), 2459–2466. doi:10.1016/j.proci.2016.08.016.

Lacaze, G., Misdariis, A., Ruiz, A., Oefelein, J.C., 2015. Analysis of high-pressure diesel fuel injection processes using LES with real-fluid thermodynamics and transport. P. Combust. Inst. 35 (2), 1603–1611. doi:10.1016/j.proci.2014.06.072.

Lemmon, E. W., Huber, M. L., McLinden, M. O., 2013. NIST standard reference database 23: reference fluid thermodynamic and transport properties-REFPROP, version 9.1.

Ma, P., Bravo, L., Ihme, M., 2014. Supercritical and transcritical real-fluid mixing in diesel engine applications. In: Proceedings of the 2014 Summer Program, Center for Turbulence Research, Stanford University.

Ma, P., Lv, Y., Ihme, M., 2016. Numerical methods to prevent pressure oscillations in transcritical flows. In: Proceedings of the 2016 Summer Program, Center for Turbulence Research, Stanford University.

Manin, J., Bardi, M., Pickett, L.M., 2012. Evaluation of the liquid length via diffused back-illumination imaging in vaporizing diesel sprays. In: The Eighth International Conference on Modeling and Diagnostics for Advanced Engine Systems (COMODIA), pp. 665–673.

Manin, J., Bardi, M., Pickett, L.M., Dahms, R.N., Oefelein, J.C., 2014. Microscopic investigation of the atomization and mixing processes of diesel sprays injected into high pressure and temperature environments. Fuel 134, 531–543. doi:10.1016/j.fuel.2014.05.060.

Masquelet, M., 2013. Large-Eddy Simulations of High-Pressure Shear Coaxial Flows Relevant for H_2/O_2Rocket Engines. Georgia Institute of Technology Ph.D. thesis.

Matheis, J., Hickel, S., 2016. Multi-component vapor-liquid equilibrium model for LES and application to ECN spray A. In: Proceedings of the 2016 Summer Program, Center for Turbulence Research, Stanford University.

Matheis, J., Müller, H., Lenz, C., Pfitzner, M., Hickel, S., 2016. Volume translation methods for real-gas computational fluid dynamics simulations. J. Supercrit. Fluids 107, 422–432. doi:10.1016/j.supflu.2015.10.004.

Matheis, J., Müller, H., Pfitzner, M., Hickel, S., 2015. Large-eddy simulation of cryogenic coaxial LN2/GH2 injection under supercritical pressures. In: Ninth International Symposium on Turbulence and Shear Flow Phenomena (TSFP-9). Melbourne.

Michelsen, M.L., 1982. The isothermal flash problem. part I. stability. Fluid Phase Equilibr. 9 (1), 1–19. doi:10.1016/0378-3812(82)85001-2.

Michelsen, M.L., Mollerup, J.M., 2007. Thermodynamic Models: Fundamentals & Computational Aspects. Tie-Line Publications.

Naber, J., Siebers, D.L., 1996. Effects of Gas Density and Vaporization on Penetration and Dispersion of Diesel Sprays. SAE Technical Paper 960034 doi:10.4271/960034.

Okong'o, N.A., Bellan, J., 2002. Consistent boundary conditions for multicomponent real gas mixtures based on characteristic waves. J. Comput. Phys. 176, 330–344. doi:10.1006/jcph.2002.6990.

Örley, F., Hickel, S., Schmidt, S.J., Adams, N.A., 2017. Large-Eddy simulation of turbulent, cavitating fuel flow inside a 9-hole diesel injector including needle movement. Int. J. Engine Res. 18 (3), 195–211. doi:10.1177/1468087416643901.

Pei, Y., Hawkes, E.R., Kook, S., Goldin, G.M., Lu, T., 2015. Modeling n-dodecane spray and combustion with the transported probability density function method. Combust. Flame 162 (5), 2006–2019. doi:10.1016/j.combustflame.2014.12.019.

Pei, Y., Som, S., Pomraning, E., Senecal, P.K., Skeen, S.A., Manin, J., Pickett, L.M., 2015. Large eddy simulation of a reacting spray flame with multiple realizations under compression ignition engine conditions. Combust. Flame 162 (12), 4442–4455. doi:10.1016/j.combustflame.2015.08.010.

Peng, D.Y., Robinson, D.B., 1976. A new two-constant equation of state. Ind. Eng. Chem. Fund. 15, 59–64. doi:10.1021/i160057a011.

Pickett, L., Kook, S., Williams, T., 2009. Visualization of diesel spray penetration, cool-flame, ignition, high-temperature combustion, and soot formation using high-speed imaging. SAE Int. J. Engines 2 (1), 439–459. doi:10.4271/2009-01-0658.

Pickett, L.M., Genzale, C.L., Manin, J., 2015. Uncertainty quantification for liquid penetration of evaporating sprays at diesel-like conditions. Atomization Sprays 25 (5), 425–452. doi:10.1615/AtomizSpr.2015010618.

Pickett, L.M., Genzale, C.L., Manin, J., Malbec, L.M., Hermant, L., 2011. Measurement uncertainty of liquid penetration in evaporating diesel sprays. In: Proceedings of the 23rd Annual Conference on Liquid Atomization and Spray Systems.

Pickett, L.M., Manin, J., Genzale, C.L., Siebers, D.L., Musculus, M.P.B., Idicheria, C.A., 2011. Relationship between diesel fuel spray vapor penetration/dispersion and local fuel mixture fraction. SAE Int. J. Engines 4 (1), 764–799. doi:10.4271/2011-01-0686.

Poling, B., Prausnitz, J., O' Connell, J., 2000. The Properties of Gases and Liquids, 5th McGraw-Hill.

Qiu, L., Reitz, R.D., 2014. Simulation of supercritical fuel injection with condensation. Int. J. Heat Mass Tran. 79, 1070–1086. doi:10.1016/j.ijheatmasstransfer.2014.08.081.

Qiu, L., Reitz, R.D., 2015. An investigation of thermodynamic states during high-pressure fuel injection using equilibrium thermodynamics. Int. J. Multiphase Flow 72, 24–38. doi:10.1016/j.ijmultiphaseflow.2015.01.011.

Qiu, L., Wang, Y., Jiao, Q., Wang, H., Reitz, R.D., 2014. Development of a thermodynamically consistent, robust and efficient phase equilibrium solver and its validations. Fuel 105, 1–16. doi:10.1016/j.fuel.2013.06.039.

Reid, R.C., Prausnitz, J.M., Poling, B.E., 1987. The Properties of Gases and Liquids, 4th McGraw-Hill.

Selle, L., Okong'o, N.A., Bellan, J., Harstad, K.G., 2007. Modelling of subgrid-scale phenomena in supercritical transitional mixing layers: an a priori study. J. Fluid Mech. 593, 57–91. doi:10.1017/S0022112007008075.

Senecal, P., Pomraning, E., 2014. Large eddy simulation of vaporizing sprays considering multi-injection averaging and grid-convergent mesh resolution. J. Eng. Gas Turbines Power 136 (11), 111504. doi:10.1115/1.4027449.

Siebers, D.L., 1999. Scaling Liquid-Phase Fuel Penetration in Diesel Sprays Based on Mixing-Limited Vaporization. SAE Technical Paper 1999-01-0528 doi:10.4271/1999-01-0528.

Star, A.M., Edwards, J.R., Lin, K.-C., Cox-Stouffer, S., Jackson, T.A., 2006. Numerical simulation of injection of supercritical ethylene into nitrogen. J. Propul. Power 22 (4), 809–819. doi:10.2514/1.16621.

Taşkinoğlu, E.S., Bellan, J., 2010. A posteriori study using a DNS database describing fluid disintegration and binary-species mixing under supercritical pressure: heptane and nitrogen. J. Fluid Mech. 645, 211. doi:10.1017/S0022112009992606.

Terashima, H., Koshi, M., 2012. Approach for simulating gas–liquid-like flows under supercritical pressures using a high-order central differencing scheme. J. Comput. Phys. 231 (20), 6907–6923. doi:10.1016/j.jcp.2012.06.021.

Terashima, H., Koshi, M., 2015. Corrigendum to "approach for simulating gas–liquid-like flows under supercritical pressures using a high-order central differencing scheme" [J. Comput. Phys. 231 (20) (2012) 6907–6923]. J. Comput. Phys. 283, 609–610. doi:10.1016/j.jcp.2014.11.013.

Wehrfritz, A., Vuorinen, V., Kaario, O., Larmi, M., 2013. Large eddy simulation of high-velocity fuel sprays: studying mesh resolution and breakup model effects for spray a. Atomization Sprays 23 (5), 419–442. doi:10.1615/AtomizSpr.2013007342.

Xue, Q., Som, S., Senecal, P.K., Pomraning, E., 2013. Large eddy simulation of fuel-spray under non-reacting IC engine conditions. Atomization Sprays 23 (10), 925–955. doi:10.1615/AtomizSpr.2013008320.